Computers and Structures 325 (2026) 108213

Contents lists available at ScienceDirect

Computers and Structures

journal homepage: www.elsevier.com/locate/cas

A frictionless contact formulation for planar multibody systems

Pietro Davide Maddio*, Rosario Sinatra, Alessandro Cammarata

University of Catania, DICAR, Via S. Sofia 64, 95123 Catania, Italy

HIGHLIGHTS

- A novel penalty formulation for 2D contact using intersection area is proposed.
- The formulation is applicable to both rigid and flexible bodies.
- Verification against the established segment-to-segment method and Hertzian theory is provided.
- The effectiveness of the formulation is demonstrated through numerical examples.

ARTICLE INFO

Keywords:
Penalty method
Contact
Flexible bodies
STS penalty formulation
Hertzian contact

ABSTRACT

A novel contact formulation for 2D flexible bodies is presented here, utilizing the penalty method. The algorithm focuses on the intersection area between the master and slave perimeters. After performing a geometric collision test, the contact force module is evaluated as a linear function of this overlapping region. The direction of the contact force is determined by computing a weighted average of the outward normal unit vectors at the boundary nodes of the contact region, where the weights account for both tributary areas and nodal indentation distances. This formulation can be applied to both rigid and flexible bodies. In the latter case, the global contact force is decomposed into the nodal forces following specific assumptions. The methodology is first compared with the Hertzian theory benchmark of two contacting cylinders. Subsequently, the method is benchmarked against the well-established segment-to-segment (STS) penalty formulation using a pin bouncing inside a journal bearing as a case study. Finally, three numerical simulations, including a standard patch test, a Geneva mechanism, and an ordinary gearbox, are studied to demonstrate the efficiency of the proposed method.

1. Introduction

The efficiency and operational lifespan of numerous mechanical systems, ranging from power transmissions and gears to cam-follower and chain-sprocket assemblies, rely heavily on the nature of contact interactions. These phenomena are omnipresent: they dictate traction and control at the tire-road interface, govern stability and noise in wheel–rail systems, and ensure the precision required for robotic grasping. Even in granular media, the collective behavior of the system is fundamentally defined by the interplay between interacting bodies.

Due to the inherent complexity of contact phenomena, closed-form solutions are restricted to idealized cases. Consequently, computational contact mechanics leverages continuum mechanics principles to investigate contact, friction, and wear through numerical methods and the discretization of bodies and interfaces [1,2]. This discretization of the contact interface has evolved into three primary methodologies: the node-to-node (NTN), node-to-segment (NTS), and segment-to-segment (STS) schemes.

The NTN scheme addresses contact boundary interfaces on a nodal basis [3,4]. It is typically reserved for interfaces with matching finite element meshes and is restricted to small deformations. Adapting this approach to large deformations or non-matching meshes necessitates continuous re-meshing to manage the addition or removal of interface nodes, increasing computational overhead.

The NTS scheme was originally conceived to manage non-matching meshes and enforce strictly geometric non-penetration conditions between contacting bodies [5–11]. Due to its straightforward implementation, intuitive physical interpretation, and versatility, it remains a standard choice in many finite element (FE) software packages. In the conventional one-pass NTS approach, the non-penetration constraint is upheld by preventing nodes on the slave boundary from penetrating the master segments; however, no reciprocal constraints are inherently

* Corresponding author.
Email address: pietro.maddio@unict.it (P.D. Maddio).

https://doi.org/10.1016/j.compstruc.2026.108213
Received 8 August 2025; Accepted 22 March 2026

Available online 28 March 2026

imposed on the master nodes. This asymmetric enforcement can compromise solution accuracy and may lead to a failure of the contact patch test unless specific corrective measures are implemented [4,12–14]. Furthermore, significant challenges arise in scenarios where identifying a unique master segment for a given slave node becomes ambiguous or computationally infeasible [15]. To address these limitations, recent advancements have introduced novel NTS algorithms integrated within the smoothed finite element (S-FEM) framework [16].

In contrast to the point-wise nature of NTS methods, the STS approach relies on a rigorous subdivision of the contact interface into discrete segments for numerical integration, paired with an independent approximation of the contact pressure [17,18]. Recently, Batistić et al. [19] utilized an STS penalty formulation within a finite volume framework to investigate planar and spatial frictional contact problems.

The STS scheme is widely regarded as the precursor to mortar finite element methods in computational mechanics. The mortar method represents an advanced numerical strategy that discretizes the contact interface through projection functions to guarantee a consistent and accurate force distribution. By enforcing compatibility and non-penetration conditions in a global, integral sense, this approach provides superior precision and robustness over traditional point-wise techniques [20–26]. Consequently, it is particularly advantageous for simulations demanding high computational fidelity and numerical stability.

In addition to the discretization approaches of the contact interface, different procedures for the enforcement of contact boundary constraints are based mainly on three methods: the penalty method, the Lagrange multiplier method, and the Augmented Lagrangian method, which is a penalized Lagrangian method, [27].

The penalty method approximates the non-penetration condition by applying a contact force proportional to penetration, avoiding extra unknowns. While simple and widely used, it requires careful tuning of the penalty parameter to avoid stiffness matrix ill-conditioning and convergence issues. The Lagrangian multiplier method exactly enforces the contact geometry conditions using extra variables defined as Lagrangian multipliers. By combining the benefits of the Lagrangian multiplier and penalty methods, the Augmented Lagrangian method provides better convergence properties compared to pure penalty methods [28].

Parallel to advancements in computational contact mechanics, modeling Flexible Multibody System Dynamics (MBSD) has become essential across engineering fields, including wind turbine gearboxes, robotics, biomechanics, and aerospace. Key research focuses on impulsive phenomena such as joint clearances, gear backlashes, and impact-driven mechanisms (e.g., object capture or ejection), where flexibility directly impacts durability and safety [29].

In MBSD, three primary modeling approaches prevail:

- Compliant Force Models: The impulsive event is modeled as a smooth force distribution, typically using spring–damper systems with linear or nonlinear stiffness [30]. This method provides a continuous representation of deformation and restitution based on material compliance and damping estimates.
- Impulse-Momentum Balance: This approach addresses velocity jump discontinuities by solving algebraic equations derived from generalized system-wide momentum balance [31]. It calculates post-impact states to update the system's velocity without modeling the contact force duration.

  Both the first and second approaches are event-driven, treating motion as piecewise smooth segments separated by switching points. A Differential Algebraic Equation (DAE) integrator handles each segment, pausing at impacts to resolve force laws before restarting with updated initial conditions.
- Nonsmooth Contact Dynamics: Unlike event-driven schemes, this time-stepping formulation directly discretizes measure differential inclusions, bypassing switching point detection [32,33]. By assuming a constant discrete state during each step, it offers a robust framework for capturing the nonsmooth nature of complex mechanical interactions.

Mixed formulations have also emerged, integrating multibody techniques with advanced contact mechanics. For instance, the Floating Frame of Reference Formulation (FFRF) has been coupled with STS techniques for transient gear dynamic simulations [34] and enhanced with hierarchically refined reduced isogeometric analysis (IGA) models [35].

Simultaneously, the Absolute Nodal Coordinate Formulation (ANCF) has proven effective for modeling thin beams undergoing large deformations. This approach has been combined with master-slave methods to simulate frictional contact dynamics [36] and extended to multi-zone contact scenarios [37]. Furthermore, Sun et al. [38] introduced a specialized STS formulation within the ANCF framework, specifically tailored for frictionless contact in planar multibody systems experiencing significant geometric nonlinearities.

The proposed method computes the global contact force between two bodies by using both the intersection area and the normal unit vectors at the nodes forming the perimeter of the contact region. The intersection area is used to determine the magnitude of the contact force, while its direction is calculated as the average of the outward normal unit vectors associated with the nodes on the intersection perimeter. The resulting force is then applied to the centroid of the contact region. The global contact force formulation enables direct application to rigid bodies. To extend the approach to flexible bodies, the contact force is decomposed into nodal forces under specific assumptions. Each nodal force is assumed to be proportional to its indentation depth and oriented along a projection vector. All nodal forces are then scaled by a factor determined to satisfy equilibrium conditions. In this way, the scale factor is the only parameter that needs to be computed, as it minimizes the residual in both force and torque balance. This strategy guarantees that all nodal forces are repulsive, without requiring iterative solvers such as Jacobi or Gauss-Seidel methods.

The main differences from the methods reported in the literature are listed below.

a) In some parts, the formulation seems more like an NTS contact approach, but with important differences. For instance, the slave body is not restricted to linear elements, as the algorithm does not rely on Lobatto integration. The issue of the smaller mesh compared to the master is also partially overcome. In the NTS contact approach, the correct sizing of elements is fundamental for a realistic transfer of stress between interacting bodies [39]. Specifically, the slave segment must be smaller than the master segment because a coarser slave mesh acting against a finer master surface often results in a numerical loss of contact. To verify that these contact stresses are being distributed correctly, a specific patch test, which serves as a numerical benchmark for accuracy, has been employed. To simplify this process and eliminate the risk of a poor manual choice, many modern finite element codes utilize a two-pass contact algorithm, performing a double check by swapping the roles of master and slave parts, ensuring a stable and accurate solution regardless of which side is assigned to each role. The proposed method is symmetric with respect to the two bodies in contact, and therefore, the definition of master and slave could also be eliminated. The classification between master and slave is maintained only for descriptive purposes to distinguish the two bodies.
b) The proposed method adopts a top-down approach, contrasting with traditional bottom-up contact formulations. In conventional techniques—such as Node-to-Node (NTN), Node-to-Surface (NTS), or Surface-to-Surface (STS)—individual contact elements are first defined and subsequently assembled using standard Finite Element Method (FEM) procedures. In our approach, however, all nodes within the intersection zone are identified during

the initial phase and treated collectively as a single contact entity. The balance of forces is enforced across the entire interface, analogous to the integral form of contact equilibrium used in segment-based methods. By directly computing the global resultant force without aggregating local components, this method proves highly efficient for simulating interactions between rigid bodies or for real-time applications, such as gaming, where high-fidelity local pressure distribution is secondary to computational speed. Furthermore, if one or both bodies are flexible, the algorithm proceeds by decomposing these global resultants across the nodes of each contact interface. This unified framework seamlessly adapts to all contact scenarios—rigid-rigid, rigid-flexible, and flexible-flexible—eliminating the need for specialized formulations like Segment-To-Analytical-Surface (STAS), [40].

c) Another key aspect is that the method finds the solution of the closest point projection (CPP) procedure without resorting to special/irregular cases. The CPP requires the differentiability of the function representing the parametrization of the contacting body's surface. At the discretization level, the discontinuity of normals is resolved by uniquely guaranteeing a contact normal at every point of the boundary.

The paper is organized as follows. Section 2 outlines the new methodology for deriving the global contact force and its subsequent decomposition into nodal forces. Next, in Section 3, the method is verified through a comparison with the Hertzian contact theory benchmark and the STS penalty formulation. Then, a patch test and two case studies are presented to validate the methodology with flexible multibody mechanisms. Finally, some concluding remarks are provided in Section 4.

2. Methodology

The proposed method calculates the contact pressure and the force between two bodies using a penalty formulation designed to be symmetrical; thus, the distinction between master and slave bodies is no longer necessary but will be maintained throughout the discussion solely to distinguish the two bodies. The latter can have multiple contacts in different areas, while self-contact cannot yet be predicted.

The method begins by meshing both the master and slave bodies with triangular finite elements. The perimeter of each body is then defined directly by the boundary nodes of this finite element mesh, where consecutive boundary nodes form the line segments that will be used for contact detection and intersection point identification. It is important to emphasize that there is no separate or additional discretization process specifically for the perimeters; rather, the boundary of the finite element mesh naturally provides the geometric representation needed for the contact algorithm. The internal nodes of the mesh are utilized when simulating flexible body dynamics, as they allow the method to capture body deformation by tracking nodal displacements throughout the simulation. However, before any penetration occurs, the algorithm must verify whether the two bodies are in contact. The process starts with a geometric inclusion test to determine whether any nodes of one body fall within the perimeter of the other body.

If none of the nodes from the master body fall inside the slave body, and vice versa, as shown in Fig. 1(a), it indicates that no contact has occurred. In this case, the algorithm advances to the next step without further computations.

If the geometric inclusion test detects that only one node, either from the master or the slave body, is located within the other, as shown in Fig. 1(b), the algorithm still bypasses the contact computation. This is because the algorithm requires at least one node from each body to identify the intersection points between the perimeters and define the intersection area, as will be explained later in the section describing the intersection point computation.

Similarly, if a node from one body lies exactly on a segment of the other, resulting in a single intersection point, the case is classified as a tangential contact, as shown in Fig. 1(c). In such cases, the algorithm skips the contact force computation, as no indentation occurs.

The step-by-step procedure for multiple area contact detection is detailed in Algorithm 1. Once the geometric inclusion test confirms that at least one node from the master and slave bodies is located inside the opposing body, the algorithm calculates the intersection points between the master and slave perimeters, as shown in Fig. 2.

This step ensures that the contact area is accurately defined, forming the basis for computing the magnitude and direction of the contact force. The intersection calculation is performed by iterating over segment pairs between the master and slave bodies. To enhance computational efficiency, the intersection checks are not performed on all segments of the master and slave perimeters. Instead, the algorithm employs a localized identification strategy to restrict the evaluation to segment pairs that are most likely to be involved in contact. Specifically, only

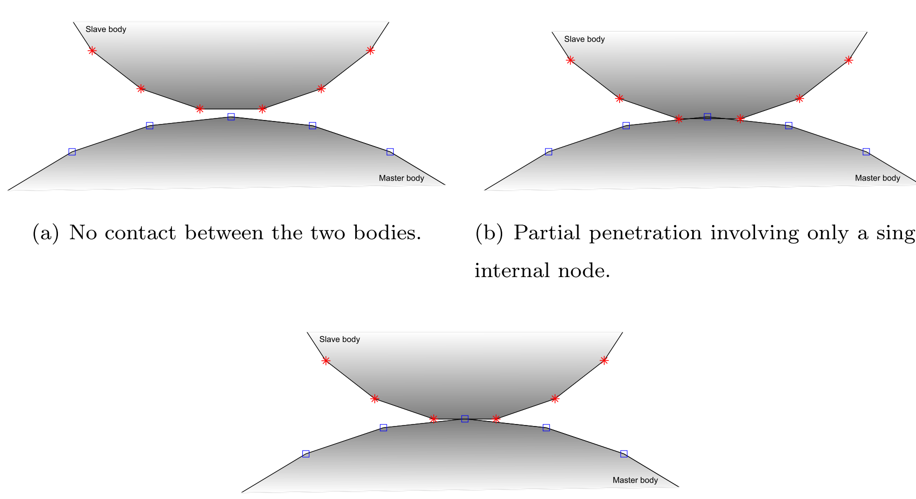

(a) No contact between the two bodies. (b) Partial penetration involving only a single internal node. (c) Tangent contact configuration.

Fig. 1. Three representative failure scenarios of the geometric inclusion test used in contact detection algorithms: (a) no contact, (b) insufficient penetration, (c) tangential contact.

Algorithm 1 Multiple area contact detection.

Require: Discretized perimeters of master and slave bodies

Find all candidate contact areas
for each contact area **do**
    Step 1: Contact detection
    Perform geometric inclusion test
    if no node from one body is inside the other **then**
        return no contact
    else if only one node lies inside the other **then**
        return insufficient penetration
    else if only one intersection point exists **then**
        return tangent contact
    else
        Valid contact configuration → Algorithm 2
    end if
end for

nodes identified by the geometric inclusion test, together with their adjacent nodes, are considered as candidates for intersection. This is because segments crossing the contact boundary necessarily connect a node inside the opposing body to one outside. The candidate segments are then constructed by connecting consecutive nodes within each expanded set, and the intersection calculation is performed only between these reduced sets of segment pairs. This selective approach significantly reduces computation time while maintaining accuracy in detecting the contact region.

For each candidate segment pair, the algorithm checks for the existence of an intersection and computes its coordinates as follows. Consider two segments: the first defined by endpoints $\mathbf{p}_1 = (x_1, y_1)$ and $\mathbf{p}_2 = (x_2, y_2)$, and the second by endpoints $\mathbf{p}_3 = (x_3, y_3)$ and $\mathbf{p}_4 = (x_4, y_4)$. The intersection point is obtained by first computing the denominator:

$$D = (x_1 - x_2)(y_3 - y_4) - (y_1 - y_2)(x_3 - x_4) \tag{1}$$

If $D = 0$, the segments are parallel and no intersection exists. Otherwise, the coordinates of the intersection point (x_i, y_i) are given by:

$$x_i = \frac{(x_1 y_2 - y_1 x_2)(x_3 - x_4) - (x_1 - x_2)(x_3 y_4 - y_3 x_4)}{D} \tag{2a}$$

$$y_i = \frac{(x_1 y_2 - y_1 x_2)(y_3 - y_4) - (y_1 - y_2)(x_3 y_4 - y_3 x_4)}{D} \tag{2b}$$

These formulas compute the intersection point of the two lines passing through the segment endpoints. However, the resulting point may lie outside the actual segments. To retain only valid intersections, the algorithm verifies that (x_i, y_i) falls within the bounding box of each segment, i.e.,:

$$\min(x_1, x_2) \le x_i \le \max(x_1, x_2) \quad \text{and} \quad \min(x_3, x_4) \le x_i \le \max(x_3, x_4) \tag{3a}$$

$$\min(y_1, y_2) \le y_i \le \max(y_1, y_2) \quad \text{and} \quad \min(y_3, y_4) \le y_i \le \max(y_3, y_4) \tag{3b}$$

Only intersection points satisfying these conditions are retained as valid.

Let n_s denote the number of slave nodes that fall within the master body, and n_m the number of master nodes that fall inside the slave body. These points, together with the intersection points of the perimeters, are then combined and ordered to define a closed polygon representing the overlapping region, as shown in Fig. 2. This polygon serves as the basis for further calculations, including the calculation of the contact area and the direction of the force.

The algorithm proceeds with the calculation of the intersection area using Gauss's area formula, a direct method for determining the area of a polygon from its vertices. Computing the intersection area is fundamental for determining the magnitude of the contact force between the master and slave bodies. Let A be the value of the intersection area, calculated using Gauss's area formula:

$$A = \frac{1}{2} \left| \sum_{i=1}^{n} \left(x_i y_{i+1} - x_{i+1} y_i \right) \right| \tag{4}$$

where $n = n_m + n_s + 2$ is the total number of vertices that define the polygon representing the area of the intersection, including the two intersection nodes. When $i = n$, Eq. (4) will contain the terms x_{n+1} and y_{n+1}; we assume $x_{n+1} = x_1$ and $y_{n+1} = y_1$ to allow the calculation of the area of closed contours.

The coordinates x_i, y_i of these vertices are ordered sequentially to form a closed polygon.

Then, the penalty method is applied to compute the global contact force. The magnitude of the force $\mathbf{F}$ is obtained by multiplying a penalty coefficient, here indicated as k_p, by the intersection area A, according to the relation:

$$|\mathbf{F}| = k_p A \tag{5}$$

In the proposed approach, the force is conceived as proportional to the intersection area, where the proportionality constant is defined by the

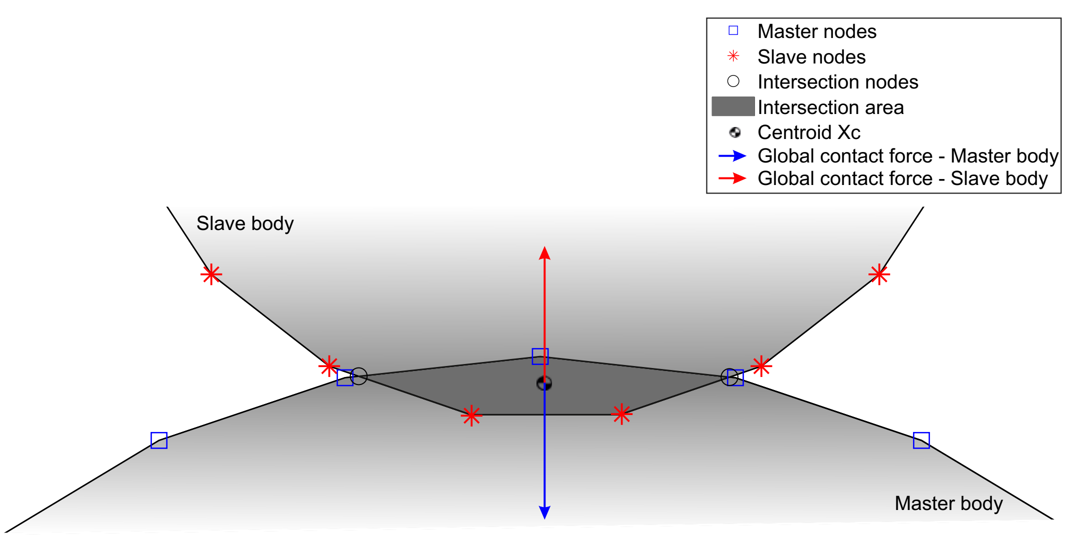

Fig. 2. Contact configuration and intersection area.

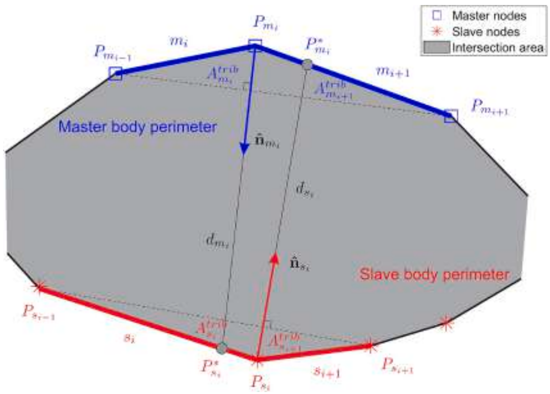

Fig. 3. Unit vector identification.

penalty coefficient k_p. Since k_p has dimensions of pressure, it is naturally scaled with respect to the equivalent elastic modulus E^* of the contacting bodies through a dimensionless factor α, i.e.

$$k_p = \alpha E^* \tag{6}$$

following a similar approach as formulated in [41]. Furthermore, a more generalized expression, $|\mathbf{F}| = f(A)$, can be formulated without loss of generality regarding the underlying methodology. The point of application of this force is set at the centroid of the overlapping region, denoted as $\mathbf{x}_c = (x_c, y_c)$, whose coordinates are calculated as:

$$x_c = \frac{1}{6A}\sum_{i=1}^{n}(x_i + x_{i+1})(x_i y_{i+1} - x_{i+1} y_i) \tag{7a}$$

$$y_c = \frac{1}{6A}\sum_{i=1}^{n}(y_i + y_{i+1})(x_i y_{i+1} - x_{i+1} y_i) \tag{7b}$$

The same point of application $\mathbf{x}_c$ is used for both the global contact forces to ensure the translational equilibrium between the two bodies, following Newton's third law.

The computation of the force direction, instead, requires a more detailed procedure. In the following, nodes will be denoted with capital italic letters while the corresponding vectors will be denoted with lower-case bold letters.

The algorithm starts by considering a generic node P_{s_i} of the slave body, $i = 1, \dots, n_s$, as shown in Fig. 3. Then, the two adjacent nodes $P_{s_{i-1}}$ and $P_{s_{i+1}}$, either internal or intersection nodes, are identified. These two nodes define a local segment whose orientation is used to compute the corresponding normal vector $\hat{\mathbf{n}}_{s_i}$ at node P_{s_i}.

The unit normal vector is calculated by rotating the vector $\mathbf{p}_{s_{i+1}} - \mathbf{p}_{s_{i-1}}$ by 90 degrees counterclockwise and normalizing the result:

$$\hat{\mathbf{n}}_{s_i} = \frac{\mathbf{R}\,(\mathbf{p}_{s_{i+1}} - \mathbf{p}_{s_{i-1}})}{\|\mathbf{p}_{s_{i+1}} - \mathbf{p}_{s_{i-1}}\|}, \quad \text{with} \quad \mathbf{R} = \begin{bmatrix} 0 & -1 \\ 1 & 0 \end{bmatrix} \tag{8}$$

Since the resulting vector may point in the opposite direction with respect to the master body, its orientation is modified to point towards the perimeter of the master body. Once the correctly oriented normal vector is obtained, the algorithm follows a directional line starting at P_{s_i} in the direction $\hat{\mathbf{n}}_{s_i}$. It then iterates over the segments of the master body m_i to find the intersection point $P^*_{m_i}$. Once this intersection is detected, the iteration stops, and the penetration distance is computed as:

$$d_{s_i} = \|\mathbf{p}_{s_i} - \mathbf{p}^*_{m_i}\| \tag{9}$$

This step is repeated for all nodes P_{s_i} of the slave body, resulting in a set of unit vectors $\hat{\mathbf{n}}_{s_i}$ and corresponding penetration distances d_{s_i}. Similarly, a corresponding set of unit vectors $\hat{\mathbf{n}}_{m_i}$, $i = 1, \dots, n_m$, is computed for the master body relative to the slave body, as shown in Fig. 3. It is noteworthy that a significant advantage of the proposed method is that it inherently resolves the Closest Point Projection (CPP) problem without requiring specific treatments for singular or irregular cases. Conventionally, the CPP procedure relies on the differentiability of the surface parametrization; however, at the discrete level, the common issue of normal discontinuities at nodes is effectively overcome. By ensuring a uniquely defined contact normal at every boundary point, the formulation maintains numerical robustness even in the presence of non-smooth geometries.

Then, the penalty formulation provides discrete nodal pressures p_i and forces $\mathbf{F}_i$ at each mesh node i located within the contact region. For a node i, the force is computed as:

$$\mathbf{F}_i = p_i A_i^{trib} \hat{\mathbf{n}}_i \tag{10}$$

where the tributary area A_i^{trib}, displayed in Fig. 3, is defined as:

$$A_i^{trib} = \frac{L_{i-1,i} + L_{i,i+1}}{2} \tag{11}$$

Here, $L_{i-1,i}$ denotes the length of the segment s_i, and $L_{i,i+1}$ denotes the length of the segment s_{i+1}. It should be noted that the intersection points, which define the boundaries of the contact region, are purely geometric entities and do not correspond to physical mesh nodes. Consequently, no contact forces or pressures are computed at these locations. For mesh nodes adjacent to an intersection point, one of the two segments in the tributary area calculation connects to this intersection point rather than to another mesh node. In a uniform mesh, segment lengths between physical nodes are approximately constant, whereas segments connecting to intersection points may have different lengths depending on the exact location of the contact boundary.

Each nodal pressure p_i, in turn, is set proportional to the q-powered distance, i.e.,

$$p_i = \alpha_s (d_{s_i})^q \tag{12}$$

where q is a coefficient that governs the shape of the resulting pressure distribution and α_s is a common scaling factor for all pressures to be determined.

The overall direction of the global contact force is then determined by aggregating all these individual forces. Specifically for the slave body, the direction of the force is given by:

$$\hat{\mathbf{F}}_s = \frac{\sum_i^{n_s} \mathbf{F}_{s_i}}{\|\sum_i^{n_s} \mathbf{F}_{s_i}\|} = \frac{\sum_i^{n_s} \alpha_s A_{s_i}^{trib}(d_{s_i})^q \hat{\mathbf{n}}_{s_i}}{\|\sum_i^{n_s} \alpha_s A_{s_i}^{trib}(d_{s_i})^q \hat{\mathbf{n}}_{s_i}\|} = \frac{\sum_i^{n_s} A_{s_i}^{trib}(d_{s_i})^q \hat{\mathbf{n}}_{s_i}}{\|\sum_i^{n_s} A_{s_i}^{trib}(d_{s_i})^q \hat{\mathbf{n}}_{s_i}\|} \tag{13}$$

which does not depend on the common scaling factor α_s. This weighted aggregation ensures that the force direction accurately reflects the contributions of all contact points. A similar expression can be found for the master body, that is,

$$\hat{\mathbf{F}}_m = \frac{\sum_i^{n_m} \mathbf{F}_{m_i}}{\|\sum_i^{n_m} \mathbf{F}_{m_i}\|} = \frac{\sum_i^{n_m} \alpha_m A_{m_i}^{trib}(d_{m_i})^q \hat{\mathbf{n}}_{m_i}}{\|\sum_i^{n_m} \alpha_m A_{m_i}^{trib}(d_{m_i})^q \hat{\mathbf{n}}_{m_i}\|} = \frac{\sum_i^{n_m} A_{m_i}^{trib}(d_{m_i})^q \hat{\mathbf{n}}_{m_i}}{\|\sum_i^{n_m} A_{m_i}^{trib}(d_{m_i})^q \hat{\mathbf{n}}_{m_i}\|} \tag{14}$$

In general, the global contact forces $\mathbf{F}_s$ and $\mathbf{F}_m$ are not in equilibrium, meaning that $\hat{\mathbf{F}}_s \neq -\hat{\mathbf{F}}_m$. To reestablish the equilibrium and make the formulation symmetric, the following strategy is adopted:

$$\hat{\mathbf{F}}_{contact} = \frac{\hat{\mathbf{F}}_s - \hat{\mathbf{F}}_m}{\|\hat{\mathbf{F}}_s - \hat{\mathbf{F}}_m\|} \tag{15}$$

Algorithm 2 Global contact force computation.

Step 2: Contact region identification
Compute intersection points between master and slave perimeters
Identify the intersection polygon
Compute the area A and the centroid $\mathbf{x}_c$
Step 3: Computation of contact force
for each contact node i of the slave/master **do**
    Identify the segment s_i, s_{i+1}, m_i, and m_{i+1}
    Compute the outward normal $\hat{\mathbf{n}}_{s_i}$ and $\hat{\mathbf{n}}_{m_i}$
    Find the intersection points $P^*_{m_i}$ and $P^*_{s_i}$
    Compute distances $d_{s_i} = \| P_{s_i} - P^*_{m_i} \|$ and $d_{m_i} = \| P_{m_i} - P^*_{s_i} \|$
    Compute the tributary areas A_{s_i} and A_{m_i}
end for
Compute force directions:

$$\hat{\mathbf{F}}_s = \frac{\sum_i^{n_s} A^{trib}_{s_i}(d_{s_i})^q \hat{\mathbf{n}}_{s_i}}{\| \sum_i^{n_s} A^{trib}_{s_i}(d_{s_i})^q \hat{\mathbf{n}}_{s_i} \|}, \quad \hat{\mathbf{F}}_m = \frac{\sum_i^{n_m} A^{trib}_{m_i}(d_{m_i})^q \hat{\mathbf{n}}_{m_i}}{\| \sum_i^{n_m} A^{trib}_{m_i}(d_{m_i})^q \hat{\mathbf{n}}_{m_i} \|}$$

Find the contact force directions

$$\hat{\mathbf{F}}_{contact} = \frac{\hat{\mathbf{F}}_s - \hat{\mathbf{F}}_m}{\|\hat{\mathbf{F}}_s - \hat{\mathbf{F}}_m\|}$$

Find the equilibrated global contact forces

$$\mathbf{F}_s = +k_p A \hat{\mathbf{F}}_{contact}, \quad \mathbf{F}_m = -k_p A \hat{\mathbf{F}}_{contact}$$

and then

$$\mathbf{F}_s = +k_p A \hat{\mathbf{F}}_{contact} \tag{16a}$$

$$\mathbf{F}_m = -k_p A \hat{\mathbf{F}}_{contact} \tag{16b}$$

These two forces are equilibrated by construction and can be directly used to implement contact for rigid bodies. The entire procedure is detailed step-by-step in Algorithm 2, which refers to both rigid and flexible bodies.

However, when studying flexible bodies, these global forces must be decomposed into individual nodal contributions according to specific criteria.

The first criterion ensures the force equilibrium, requiring the sum of all nodal forces to equal the global contact force:

$$\sum_{i=1}^{n_s} \mathbf{F}_{s_i} = \mathbf{F}_s \tag{17}$$

The second criterion ensures the torque equilibrium and requires that the sum of the moments of the individual nodal forces, calculated with respect to the centroid $\mathbf{x}_c$, is zero:

$$\sum_{i=1}^{n_s} \bar{\mathbf{a}}^T_{s_i} \mathbf{F}_{s_i} = 0 \tag{18}$$

where $\mathbf{a}_{s_i} = \mathbf{p}_{s_i} - \mathbf{x}_c$ represents the distance between the i-th node of the slave body and the centroid of the overlapping area and $\bar{\mathbf{a}}_{s_i}$ is obtained as $\bar{\mathbf{a}}_{s_i} = \hat{\mathbf{k}} \wedge \mathbf{a}_{s_i}$, with $\hat{\mathbf{k}}$ being the unit vector normal to the plane of interaction.

In general, combining Eqs. (17) and (18), a linear problem with n_s unknowns F_{s_i}, $i = 1 \dots n_s$, is obtained. Since this is an under-constrained problem, infinite solutions exist. Furthermore, the solution of the system can provide negative values for the magnitudes F_{s_i}, thereby producing an unfeasible physical interpretation as the negative values would represent attractive forces. One possible approach to overcome this issue involves ensuring that all nodal forces are non-negative, e.g., repulsive forces, as is done using iterative solvers such as Jacobi or Gauss-Seidel methods [33]. However, this approach can result in an unfeasible force distribution.

Instead, following Eqs. (10) and (12), we assigned to each nodal force a magnitude F_{s_i} defined as

$$F_{s_i} = \alpha_s (d_{s_i})^q A^{trib}_{s_i} \tag{19}$$

where α_s is the only unknown to be determined. Following this strategy, the resulting nodal forces are guaranteed to be positive, as their direction is defined by the unit vectors $\hat{\mathbf{n}}_{s_i}$ while their magnitude is expressed in absolute value. Furthermore, each nodal contact force is proportional to the local indentation within the contact area; therefore, nodes with smaller indentation contribute less to the overall force. This behavior can be further tuned by adjusting the parameter q. In particular, by increasing q more weight will be given to the nodes with the highest penetration.

By inserting Eq. (10) into Eq. (17) and factoring out the scaling factor α_s, the global contact force can be reformulated as

$$\alpha_s \sum_{i=1}^{n_s} A^{trib}_{s_i}(d_{s_i})^q \hat{\mathbf{n}}_{s_i} = \mathbf{F}_s \tag{20}$$

Similarly, Eq. (18) turns into the following

$$\alpha_s \sum_{i=1}^{n_s} \bar{\mathbf{a}}^T_{s_i} A^{trib}_{s_i}(d_{s_i})^q \hat{\mathbf{n}}_{s_i} = 0 \tag{21}$$

These two equations can be reformulated in matrix form:

$$\alpha_s \mathbf{B}_s = \mathbf{b}_s \tag{22}$$

where the $3 \times n_s$ matrix $\mathbf{B}_s$ and the 3-dimensional vector $\mathbf{b}_s$ are defined as:

$$\mathbf{B}_s = \begin{bmatrix} A^{trib}_{s_1}(d_{s_1})^q \hat{\mathbf{n}}_{s_1} & \cdots & A^{trib}_{s_{n_s}}(d_{s_{n_s}})^q \hat{\mathbf{n}}_{s_{n_s}} \\ \bar{\mathbf{a}}^T_{s_1} A^{trib}_{s_1}(d_{s_1})^q \hat{\mathbf{n}}_{s_1} & \cdots & \bar{\mathbf{a}}^T_{s_{n_s}} A^{trib}_{s_{n_s}}(d_{s_{n_s}})^q \hat{\mathbf{n}}_{s_{n_s}} \end{bmatrix}, \quad \mathbf{b}_s = \begin{bmatrix} \mathbf{F}_s \\ 0 \end{bmatrix} \tag{23}$$

The same procedure can be implemented for the master nodes, leading to

$$\alpha_m \mathbf{B}_m = \mathbf{b}_m \tag{24}$$

where the $3 \times n_m$ matrix $\mathbf{B}_m$ and the 3-dimensional vector $\mathbf{b}_m$ are defined as:

$$\mathbf{B}_m = \begin{bmatrix} A^{trib}_{m_1}(d_{m_1})^q \hat{\mathbf{n}}_{m_1} & \cdots & A^{trib}_{m_{n_m}}(d_{m_{n_m}})^q \hat{\mathbf{n}}_{m_{n_m}} \\ \bar{\mathbf{a}}^T_{m_1} A^{trib}_{m_1}(d_{m_1})^q \hat{\mathbf{n}}_{m_1} & \cdots & \bar{\mathbf{a}}^T_{m_{n_m}} A^{trib}_{m_{n_m}}(d_{m_{n_m}})^q \hat{\mathbf{n}}_{m_{n_m}} \end{bmatrix}, \quad \mathbf{b}_m = \begin{bmatrix} \mathbf{F}_m \\ 0 \end{bmatrix} \tag{25}$$

The two systems (22) and (24) have α_s and α_m as their only unknowns, respectively. In the proposed model, the parameter α scales all contact pressures while preserving the same shape of the pressure distribution, thereby adapting it to balance the global contact force.

The complete procedure is summarized in Algorithm 3, which specifically pertains to flexible bodies as it handles the derivation of both nodal pressures and forces. For both rigid and flexible bodies, the algorithm necessitates a boundary mesh of the two contacting entities. In the case of a rigid body, calculating the global force applied at the centroid of the contact area is sufficient to determine the system's dynamic response. Conversely, for flexible bodies, the global forces are further decomposed into nodal contributions, provided the boundary mesh is a subset of the overall surface mesh. It should be noted that the FFRF method used for the equations of motion requires not only these nodal components but also the global force and its corresponding moment relative to the FFR origin.

Algorithm 3 Nodal pressure and forces.

1: Form the two linear systems and solve for α_s and α_m:

$$\alpha_s \mathbf{B}_s = \mathbf{b}_s, \quad \alpha_m \mathbf{B}_m = \mathbf{b}_m$$

2: Recover nodal pressures:

$$p_{s_i} = \alpha_s (d_{s_i})^q, \quad p_{m_i} = \alpha_m (d_{m_i})^q$$

3: Recover nodal forces:

$$\mathbf{F}_{s_i} = p_{s_i} A^{trib}_{s_i} \hat{\mathbf{n}}_{s_i}, \quad \mathbf{F}_{m_i} = p_{m_i} A^{trib}_{m_i} \hat{\mathbf{n}}_{m_i}$$

4: Create the generalized contact forces for each area j:

$$\mathbf{Q}_{s_j} = \begin{bmatrix} \mathbf{F}_s^T | & \cdots & \mathbf{F}_{s_1}^T & \mathbf{F}_{s_2}^T & \cdots & \mathbf{F}_{s_{n_s}}^T & \cdots \end{bmatrix}^T$$
$$\mathbf{Q}_{m_j} = \begin{bmatrix} \mathbf{F}_m^T | & \cdots & \mathbf{F}_{m_1}^T & \mathbf{F}_{m_2}^T & \cdots & \mathbf{F}_{m_{n_m}}^T & \cdots \end{bmatrix}^T$$

5: Find the global vector of generalized contact forces:

$$\mathbf{Q}_i = \sum_{j=1}^{n_{area}} \begin{bmatrix} \cdots & \mathbf{Q}_{s_j}^T & \cdots & \mathbf{Q}_{m_j}^T & \cdots \end{bmatrix}^T$$

2.1. DAE system

Following the formulation proposed in [34], the contact forces are incorporated into the Differential Algebraic Equation (DAE) system which contains the equations of motion and the nonlinear constraints, i.e.,

$$\begin{cases} \mathbf{M}(\mathbf{q})\ddot{\mathbf{q}} + \mathbf{\Phi}_q^T(\mathbf{q})\lambda + \mathbf{D}\dot{\mathbf{q}} + \mathbf{K}\mathbf{q} = \mathbf{Q}_v(\mathbf{q}, \dot{\mathbf{q}}) + \mathbf{Q}_i(\mathbf{q}) \\ \mathbf{\Phi}(\mathbf{q}) = \mathbf{0} \end{cases} \tag{26}$$

where

- $\mathbf{q}$: generalized coordinates
- λ: mechanical constraint Lagrange multipliers
- $\mathbf{M}(\mathbf{q})$: generalized mass matrix
- $\mathbf{\Phi}_q$: Jacobian of the constraints
- $\mathbf{D}$: generalized damping matrix
- $\mathbf{K}$: generalized stiffness matrix
- $\mathbf{Q}_v$: generalized vector of Coriolis/centrifugal forces
- $\mathbf{Q}_i$: generalized contact forces

System (26) is then integrated using the generalized-α method provided in [42]. To speed up computation, each flexible component has been reduced using normal modes obtained by imposing free-floating reference conditions [43], and system (26) is converted into its reduced form.

3. Numerical simulations

The methodology is first verified using the contact between two cylinders, a classic benchmark of Hertzian theory. Subsequently, four case studies are examined: a planar pin joint, a patch test, a Geneva mechanism, and a conventional gearbox. For all scenarios, a global search phase was implemented, utilizing distance checks or axis-aligned bounding box (AABB) intersections to identify potential contact pairs. Once a collision is detected during the global search, a local search is triggered to precisely calculate the intersection areas and identify the specific perimeter segments involved in the contact.

3.1. Hertz theory benchmark: two cylinders pressed into contact

To evaluate the accuracy of the proposed penalty-based contact formulation, a benchmark problem with a known analytical solution was investigated. The classical Hertzian contact theory for two elastic cylinders with parallel axes serves as an ideal reference, providing closed-form expressions for both the contact half-width and the pressure distribution [44].

Consider two elastic cylinders with parallel axes, radii R_1 and R_2, and identical material properties characterized by Young's modulus E and Poisson's ratio ν. When the cylinders are pressed together by a force per unit length F, the contact occurs along a narrow rectangular strip of half-width a. The equivalent relative curvature is defined as:

$$\frac{1}{R^*} = \frac{1}{R_1} + \frac{1}{R_2} \tag{27}$$

which, for the case of equal radii $R_1 = R_2 = R$, allows for calculating the equivalent radius $R^* = R/2$. The plane-strain equivalent modulus is given by:

$$E^* = \frac{E}{2(1-\nu^2)} \tag{28}$$

According to Hertzian theory [44], the contact half-width is expressed as:

$$a = \sqrt{\frac{4FR^*}{\pi E^*}} \tag{29}$$

The resulting pressure distribution within the contact region $x \in [-a, a]$ exhibits a semi-elliptical profile:

$$p(x) = \frac{2F}{\pi a^2}\sqrt{a^2 - x^2} \tag{30}$$

with a maximum value at the center of the contact zone:

$$p_{\max} = p(0) = \frac{2F}{\pi a} \tag{31}$$

A two-dimensional contact problem involving two cylinders of equal radius $R = 8$ m was investigated [19]. Both bodies are assumed to be linearly elastic, with a Young's modulus $E = 200$ Pa and a Poisson's ratio $\nu = 0.3$. While these parameters do not represent typical engineering materials, they were deliberately selected to produce contact dimensions of order unity, thereby facilitating the numerical verification process.

The applied load was set to $F = 10$N. Substituting the relevant parameters into Eq. (29) yields a ≈ 0.97 m.

To establish conditions consistent with the Hertzian assumptions, the vertical separation between the centers of the cylinders was adjusted so that the geometric intersection of the undeformed bodies coincided precisely with the theoretical contact boundaries at $x = \pm a$. This procedure ensures that the penalty-based algorithm operates over a contact region identical to that predicted by the analytical solution.

Within the proposed penalty framework, the global contact force is computed as:

$$F = k_p A \tag{32}$$

where k_p denotes the penalty stiffness and A represents the overlapping area between the contacting bodies. To reproduce the target load of $F = 10$N, the penalty coefficient was determined as:

$$k_p = \frac{F_{target}}{A} \tag{33}$$

where A is evaluated at runtime based on the actual geometric intersection. This calibration strategy ensures force consistency between the numerical and analytical solutions.

Regarding the value of the distance exponent q, it is set equal to 0.5 so that the pressure law in Eq. (9) recovers the semi-elliptical Hertzian distribution. As shown analytically by Johnson [44], this is the unique value consistent with the parabolic approximation of the gap between cylindrical surfaces.

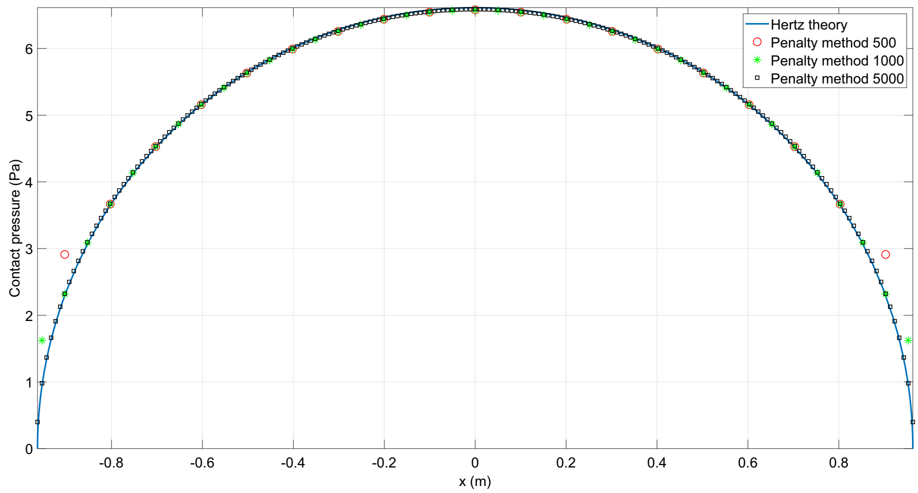

Fig. 4. Contact pressure distribution: comparison between the analytical Hertzian solution (solid blue line) and the penalty-based numerical method with $q = 0.5$ and different mesh sizes (500, 1000, 5000).

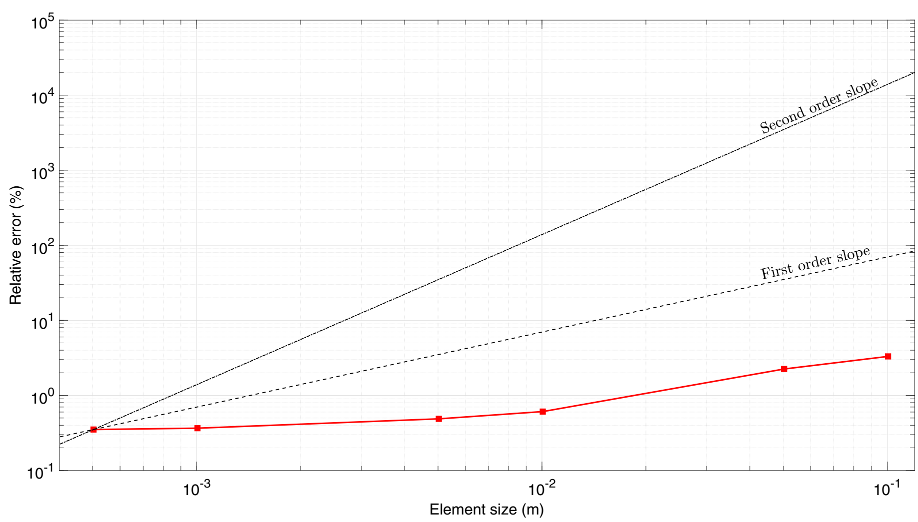

Fig. 5. Mesh sensitivity analysis: relative error in maximum contact pressure as a function of the element size.

Fig. 4 presents the pressure distribution obtained from the penalty method for three different mesh densities, equal to 500, 1000, and 5000 nodes, alongside the analytical Hertzian solution. The numerical results exhibit remarkable agreement with the theoretical prediction across the entire contact region, with all three discretizations closely following the characteristic semi-elliptical profile.

Quantitative assessment of the numerical accuracy was performed by evaluating the relative error at the center of the contact zone, as shown in Fig. 5, where the maximum pressure occurs:

$$\varepsilon = \frac{|p_{\max}^{penalty} - p_{\max}^{Hertz}|}{p_{\max}^{Hertz}} 100 \tag{34}$$

The theoretical maximum pressure, computed from Eq. (31), is:

$$p_{\max}^{Hertz} = \frac{2F}{\pi a} \approx 6.61\text{Pa} \tag{35}$$

The corresponding value obtained from the penalty method was $p_{\max}^{penalty} \approx 6.59$Pa, resulting in a relative error of $\varepsilon \approx 0.37\%$. This close agreement verifies the proposed penalty-based contact algorithm and confirms its capability to accurately reproduce the classical Hertzian pressure distribution.

The small discrepancy observed near the contact boundaries can be attributed to the discrete nature of the mesh and the finite size of the tributary areas near the intersection points; mesh refinement is expected to reduce this error further.

3.2. Planar pin-joint

To evaluate the effectiveness of the proposed formulation, a numerical simulation is performed on a planar pin-joint. The system consists of a circular pin with radius $R_1 = 20$ (mm), designated as the slave body, placed inside a concentric circular support with radius $R_2 = 35$ (mm), chosen as the master body, so that, at initial time $t = 0$, the two bodies share the same center, as shown in Fig. 6.

The pin and the support are modeled as linear elastic bodies. Structural parameters and penalty coefficients are reported in Table 1.

The inner pin is subjected to gravitational loading, which causes the pin to move downward within the circular cavity of the support. As the simulation progresses, the pin gradually loses its initial alignment and comes into contact with the lower portion of the housing. The goal of the analysis is to capture the evolution of the contact interaction over a defined time interval $t \in [0, T]$, focusing on both the distribution and the magnitude of the forces exchanged between the two bodies. This

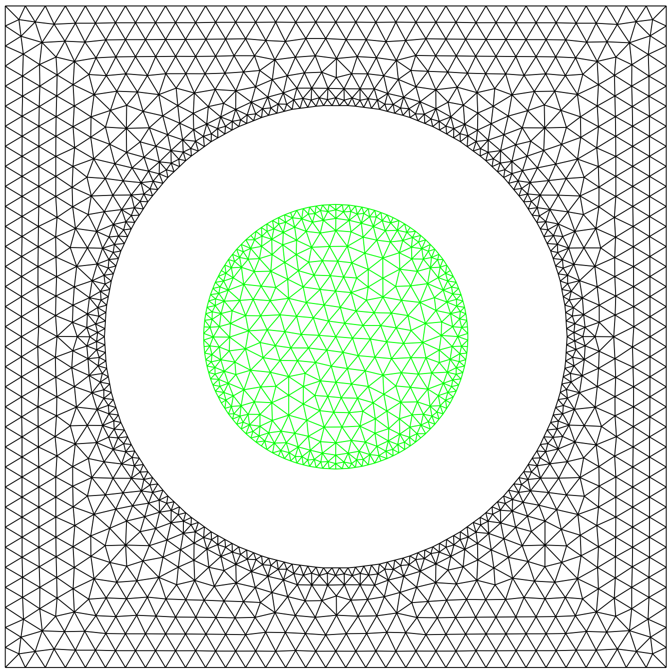

Fig. 6. Initial position of the planar pin-joint. The circular pin, acting as the slave body, is shown in green and is initially centered within the circular support, shown in black, which serves as the master body.

Table 1
Pin-joint structural parameters.

Young module E (Pa)	Poisson ratio ν	thickness t (mm)	mass density ρ (kg/m^3)	penalty coefficient k_p
207×10^8	0.29	5	7800	5×10^7

configuration serves as a benchmark for verification, as it allows a direct comparison between the results obtained using the proposed method and those produced by the well-established STS formulation. At the beginning of the numerical simulation, the first contact event occurs when at least one node from the master body and one node from the slave body penetrate beyond the perimeter of the opposing body. As described in Section 2, this condition activates the contact algorithm, which calculates both the centroid and the area of the overlapping region. At each time step, the contact force is computed and subsequently distributed among the nodes involved in the penetration region for both the master and slave bodies. This process continues until the contact force reaches its maximum value, corresponding to the time instant t^* when the two bodies reach their maximum penetration. After the compression phase, the restitution phase begins as the pin rebounds, and the contact force gradually decreases as the bodies separate, eventually returning to their initial configuration.

Fig. 7 shows the configuration corresponding to the maximum penetration with a mesh size of 1.0 (mm). The nodal contact forces for the slave body are shown in red, and those for the master body are shown in blue, using both the STS formulation and the proposed method. It can be observed that the force distributions are remarkably similar in both formulations, characterized by a bell-shaped profile that reflects the extent of penetration between the bodies.

To assess the robustness of the proposed method with respect to mesh density, additional simulations were performed using two different mesh spacings: a finer mesh size of 0.7 (mm) and a coarser mesh size of 1.3 (mm). Figs. 8 show the nodal contact force distributions at maximum penetration for both mesh configurations. The comparison demonstrates that the proposed approach maintains excellent agreement with the STS formulation across different levels of discretization.

Table 2 reports the computational times for the three mesh densities considered. The results demonstrate that the proposed approach achieves significantly shorter simulation times across all mesh densities, with computational savings ranging from approximately 46% to 51%. It should be noted that this comparison was conducted using a common code framework for both methods, which differ only in the calculation of contact forces. All parameters related to simulation time, time step, and convergence tolerance of the generalized-alpha method were set equally for both formulations, ensuring a fair comparison. The computational advantage is maintained consistently across different mesh refinement levels, indicating good scalability of the proposed method.

The effectiveness of the proposed method is further confirmed by comparing the evolution of the global contact force with that obtained using the STS formulation. Fig. 9 illustrates this comparison, focusing on the time interval spanning from the initial contact event to the instant of body separation. The two curves are nearly indistinguishable, highlighting the excellent agreement between the two formulations.

Another indicator of the effectiveness of the proposed method can be observed in Fig. 10, which illustrates the time evolution of the

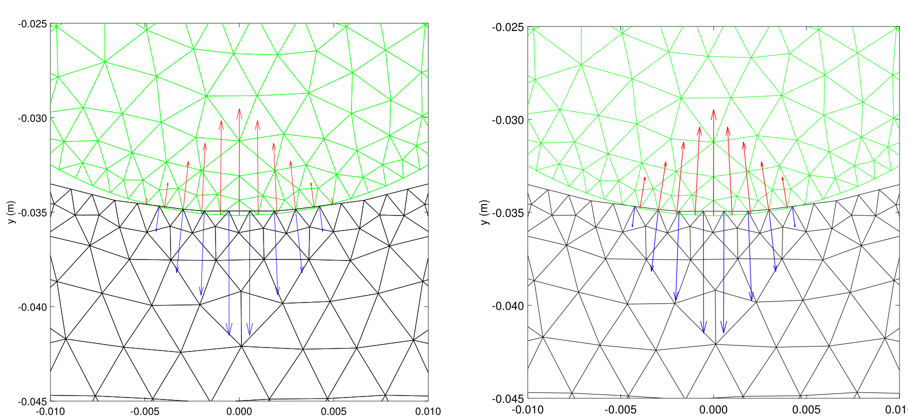

(a) STS method, mesh size=1.0 (mm). (b) Proposed method, mesh size=1.0 (mm).

Fig. 7. Comparison of nodal contact forces computed using (a) the STS formulation and (b) the proposed method with mesh size = 1 (mm). Red arrows indicate the nodal contact forces on the slave body, while blue arrows correspond to those on the master body. The results show strong agreement in both the trend and magnitude of the computed forces for the two formulations.

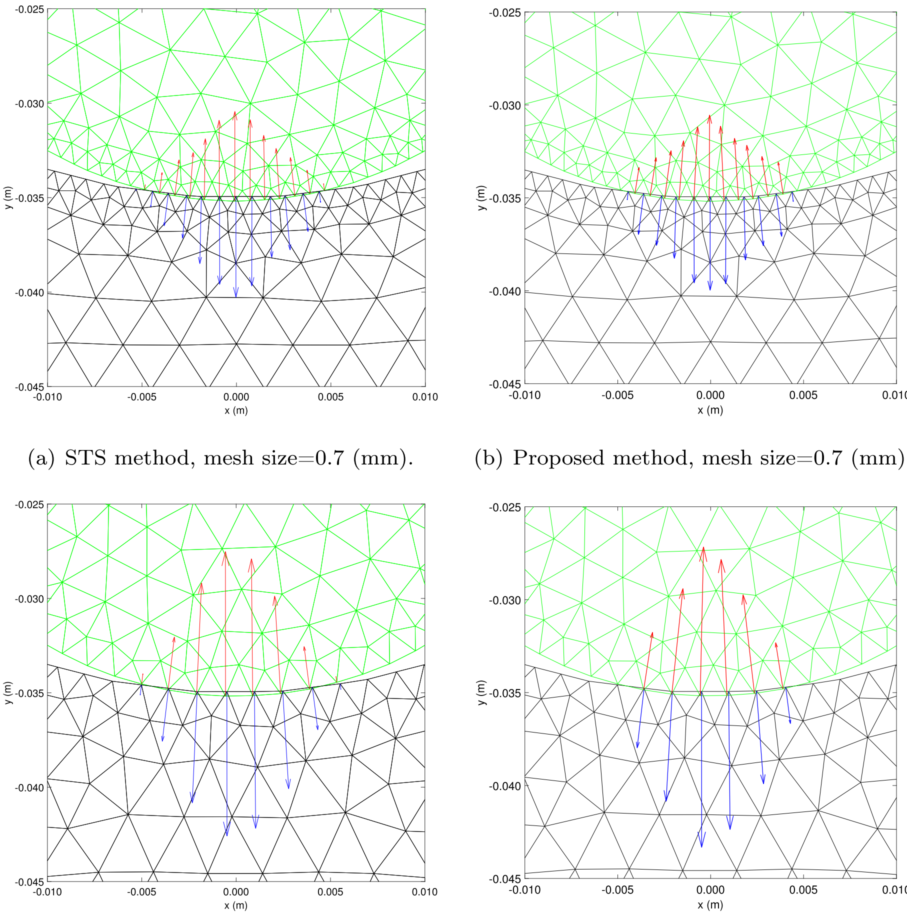

(a) STS method, mesh size=0.7 (mm).

(b) Proposed method, mesh size=0.7 (mm).

(c) STS method, mesh size=1.3 (mm).

(d) Proposed method, mesh size=1.3 (mm).

Fig. 8. Comparison of nodal contact forces for two mesh densities: (a)–(b) mesh size of 0.7 (mm) and (c)–(d) mesh size of 1.3 (mm).

Table 2
Computational time comparison between the STS formulation and the proposed method for different mesh sizes.

Mesh size (mm)	STS method (s)	Proposed method (s)
0.7	21.61	11.57
1.0	19.05	9.29
1.3	16.57	8.99

vertical displacement of the slave body over the interval $t \in [0, 0.3]$ (s). Specifically, the figure shows the vertical trajectory of the center of mass of the pin. After the first contact, corresponding to the minimum point, i.e., the moment of maximum penetration, approximately after $t = 0.05$ (s), the pin returns to its initial position at $y = 0$, confirming that the method does not introduce dissipation when included in an implicit time-stepping scheme such as the Generalized-alpha method. This behavior is repeated in subsequent bounces. In particular, and in agreement with the results shown in Fig. 9, the two formulations exhibit an almost perfect overlap, further confirming the accuracy of the proposed contact algorithm.

3.3. Patch test

The patch test is a benchmark used in computational contact mechanics to assess the accuracy of a contact algorithm in transmitting uniform stress between two contacting bodies. This test is crucial for verifying the robustness of penalty-based contact models. Taylor and Papadopoulos originally introduced the patch test [4] as a criterion to ensure that a contact formulation can accurately transfer constant normal stress across the contact interface.

In the execution of this patch test, two rectangular bodies are arranged so that their surfaces remain parallel, thus maintaining a uniform gap. For ease of description, the larger rectangle will be considered the master body, while the smaller one will be the slave. The bottom surface of the master body is fully constrained, whereas the slave body is initially positioned slightly above the master and then released under the action of gravity. As the slave body falls and comes into contact with the master, the contact algorithm is activated, and the resulting pressure distribution is evaluated.

First, the true patch-test case with uniform mesh discretization is performed by imposing forces to the upper body. As shown in Fig. 11, a uniform distribution of contact pressure occurs in both the master and slave bodies. The edge nodes have smaller forces because their tributary area is smaller than that of the internal nodes, calculated by considering the previous/next internal nodes, along with the intersection point, as adjacent nodes.

Fig. 12 reports the corresponding contact pressure distribution along the interface for both the master and slave bodies. The pressure values are nearly uniform across the contact region, with variations on the order of 10^{-2} (Pa). The small discrepancy between the two values is related to the tributary area distribution discussed above for the edge nodes: the slave body has a slightly larger total tributary area along the contact interface, as it includes contributions from the vertical sides of

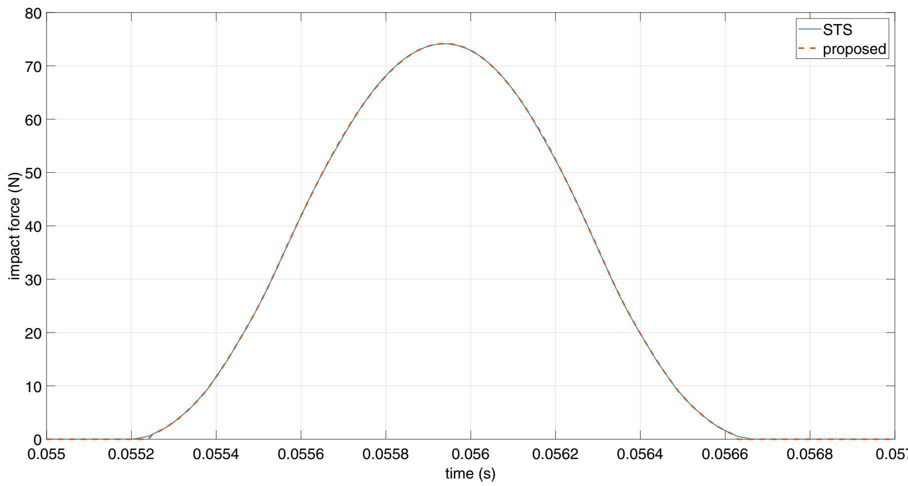

Fig. 9. Evolution of the global contact force over time, comparing the results of the proposed formulation with those obtained using the STS approach. The plot refers to the time interval spanning from the initial contact to the loss of interaction between the two bodies.

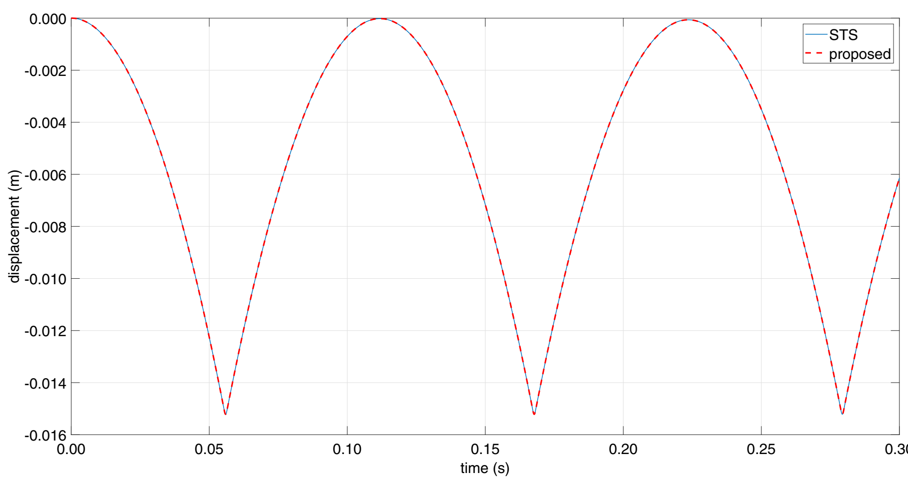

Fig. 10. Vertical displacement of the slave body's center of mass over time, comparing the proposed method and the STS formulation.

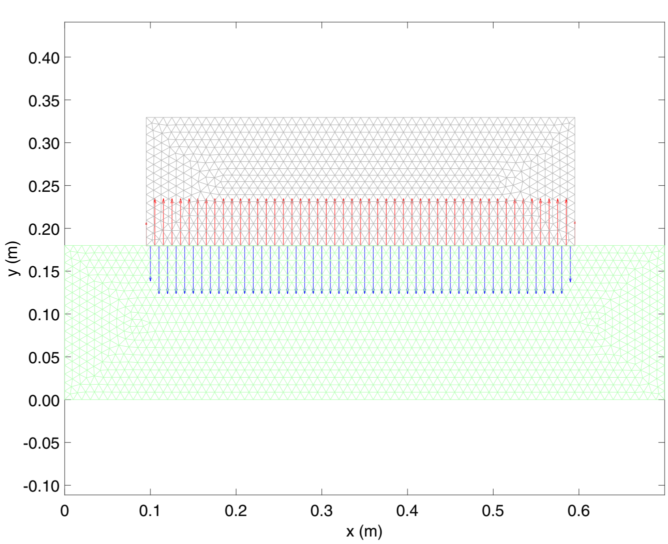

Fig. 11. Patch test setup. The master body (green) is constrained, while the slave body (gray) is released under gravity. Nodal contact forces are shown in blue (master) and red (slave).

the penetrating portion in addition to the horizontal interface. This effect decreases as the contact gap is reduced.

To investigate the role of the gap and node distribution, four cases were simulated by imposing prescribed displacements: they are divided into two pairs with gaps set to 2 (mm) and 6 (mm), respectively. For each gap, two cases are presented: the first with a defined non-uniform mesh and the second with a mesh obtained from a random distribution.

The results are presented in Fig. 13. First, it is observed that the force distribution follows the nodal arrangement, as it is directly governed by the calculation of the tributary areas. This behavior accurately reflects the physics of the contact process: an increase in nodal density results in smaller tributary areas, consequently reducing individual nodal forces. Conversely, regions with a lower nodal density exhibit higher forces due to their larger associated tributary areas.

Second, while the contact pressure remains uniform across each body, a discrepancy exists between the two values. This discrepancy arises from the asymmetrical positioning of the intersection nodes; specifically, while the slave nodes are aligned along the contact interface, this alignment is not maintained for the master nodes.

3.4. Geneva mechanism

A planar Geneva mechanism is presented further to verify the capabilities of the proposed contact algorithm. The Geneva drive is a widely

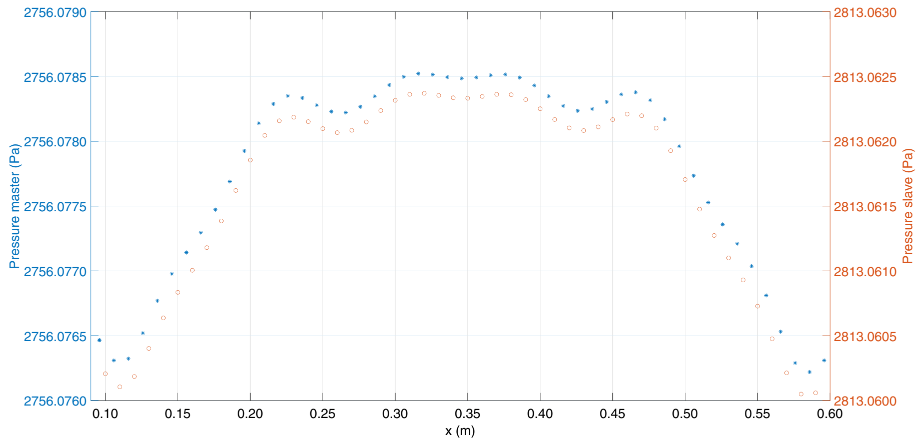

Fig. 12. Contact pressure at each boundary node along the interface for the master (blue) and slave (red) bodies.

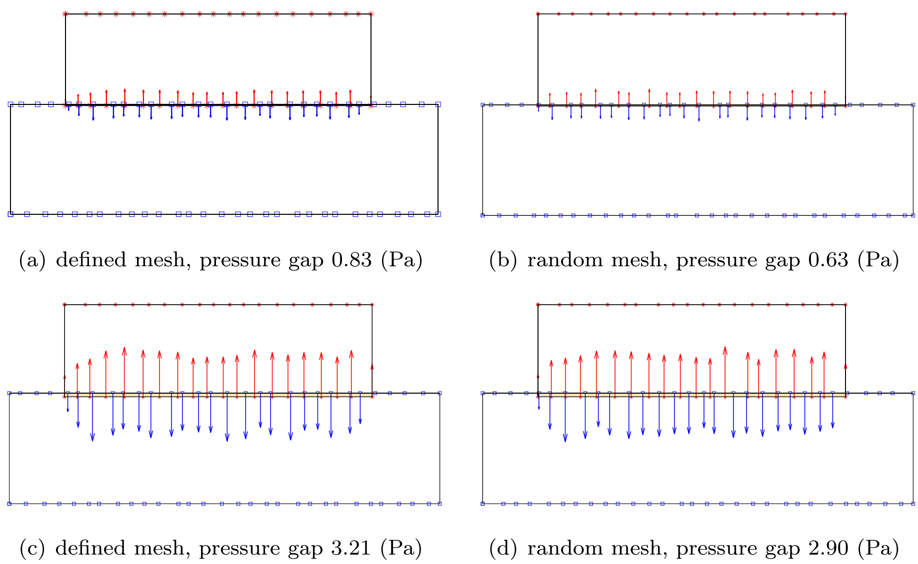

Fig. 13. Figures (a) and (b) report the nodal contact forces considering a gap of 2 (mm). Figures (c) and (d) report the nodal contact forces considering a gap of 6 (mm).

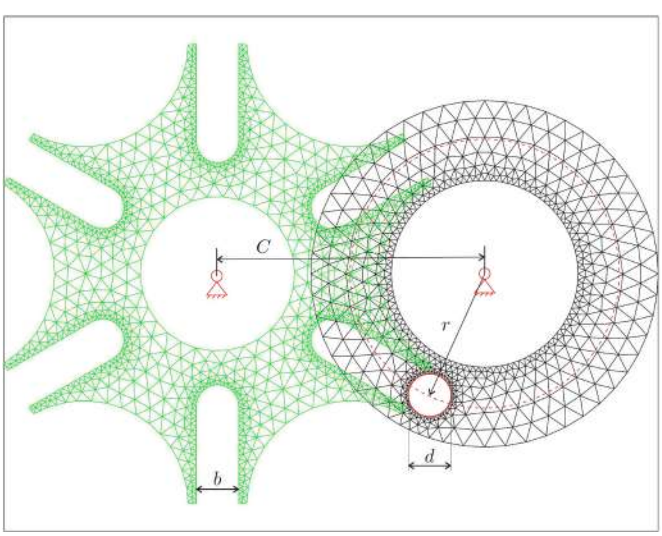

Fig. 14. Initial configuration of the Geneva mechanism. The driving wheel, equipped with a pin, is shown in black, while the driven wheel, equipped with the six equally spaced radial slots, is shown in green.

used indexing mechanism that converts continuous rotational motion into intermittent rotary motion. It consists of a driving wheel equipped with a pin and a driven wheel containing a set of radial slots. The pin enters one slot at a time at specific intervals, resulting in discrete rotational steps of the driven wheel.

Fig. 14 shows the initial configuration of the mechanism, where the pin of the driving wheel, shown in green, is positioned immediately before engaging one of the radial slots of the driven wheel, which is represented in black. In a Geneva mechanism with n slots, the center distance C and the crank radius r are related by the engagement requirement

$$m = \frac{r}{C} = \sin\left(\frac{\pi}{n}\right) \tag{36}$$

The instantaneous distance $\rho(\theta)$ between the driven wheel center and the pin center is

$$\rho(\theta) = \sqrt{C^2 + r^2 - 2Cr\cos\theta} \tag{37}$$

The theoretical angular position of the driven wheel ϕ is given by

$$\phi = \mathrm{atan2}(r\sin\theta, C - r\cos\theta)] \tag{38}$$

Table 3
Geneva mechanism geometrical parameters.

wheelbase C (mm)	driver radius r (mm)	pin diameter d (mm)	slot width b (mm)	clearance g (mm)
50	25	8	8.01	0.01

Table 4
Geneva mechanism structural parameters.

Young module E (Pa)	Poisson ratio ν	thickness t (mm)	mass density ρ (kg/m^3)	penalty coefficient k_p
207×10^8	0.29	5	7800	6×10^8

However, to ensure correct operation, it is necessary to provide a clearance g between the width b of the slots and the diameter d of the pin. Assuming the pin maintains contact with the slot wall, the clearance g introduces an angular error $\Delta\phi(\theta)$, i.e.,

$$\Delta\phi(\theta) = \arcsin\left(\frac{g/2}{\rho(\theta)}\right) \tag{39}$$

Due to clearance, the effective angular position of the driven wheel ϕ_{eff} becomes

$$\phi_{eff}(\theta) = \phi \pm \Delta\phi(\theta) \tag{40}$$

where the sign of the correction depends on the direction of rotation: negative for counterclockwise rotations and positive for clockwise ones.

Fig. 14 also describes the starting condition of the simulation, while the mechanism's geometrical, inertial, and structural parameters are reported in Tables 3 and 4. Since the driven wheel has six radial slots, each full revolution of the driving wheel produces a discrete rotation of $\pi/3$ radians of the driven wheel.

In the proposed configuration, the driving wheel rotates at a constant angular velocity. During this interaction phase, contact occurs between the cylindrical surface of the pin and the perimeter of the radial slot. As in the previous test cases, both bodies are modeled as flexible and equipped with revolute joints modeled using RBE3 elements, which allow each flexible body to rotate about its center while preserving local deformation at the interface. The driving wheel is subjected to a rheonomic constraint, rotating at a constant angular velocity. In contrast, the driven wheel is free to rotate under the action of the contact forces. To ensure its angular stability during disengagement phases and to prevent undesired backward motion, a torsional damper of constant $d = 0.1$ N m s/rad was introduced at the center of the driven wheel. This addition helps maintain the wheel close to its target position, minimizing the risk of misalignment during subsequent engagements.

This numerical simulation is particularly significant because of the dynamic nature of the interaction, which involves repeated cycles of contact engagement and disengagement. These characteristics make the Geneva mechanism an ideal benchmark for assessing the performance of contact formulations under intermittent and nonconforming contact conditions.

Fig. 15 shows the angular displacement of the driven wheel over a simulation time of 10 s. The driving wheel is set to rotate at a constant angular velocity of 30 (rpm). As can be observed, the rotation of the driven wheel occurs in discrete steps of $\pi/3$ radians, confirming expectations.

In Fig. 16, the comparison between the effective angular position of the driven wheel with the proposed method using a simulation time of 1 s. Considering the starting conditions and the presence of clearance g, contact should theoretically occur at a time $t = 0.0329$. However, in the proposed method, contact does not occur at the point of tangency between the pin and slot but is slightly shifted in time, i.e., $t = 0.0414$, due to the penetration of the profiles, which has the same effect as an increased clearance compared to the actual one. This phenomenon generates a delay in the rotation of the driven element, as can be seen from the phase shift of the two curves. It is important to emphasize that this phenomenon cannot be eliminated in a penalty method.

Despite this inherent phase shift due to contact detection delay, the overall kinematic accuracy was quantitatively verified by computing the normalized RMS error between the simulated ϕ_{sim} and the effective ϕ_{eff} angular positions over the engagement phase:

$$\varepsilon_\phi = \frac{1}{\phi_{\text{eff}}}\sqrt{\frac{1}{n}\sum_{i=1}^{n}(\phi_{\text{sim},i} - \phi_{\text{eff},i})^2} \times 100 = 1.13\% \tag{41}$$

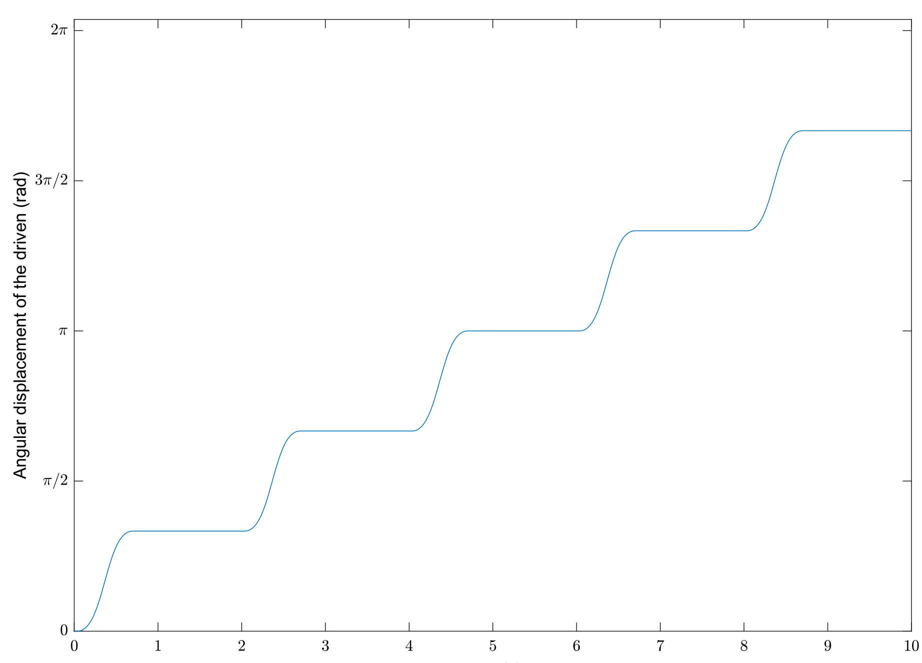

Fig. 15. Angular displacement of the driven wheel.

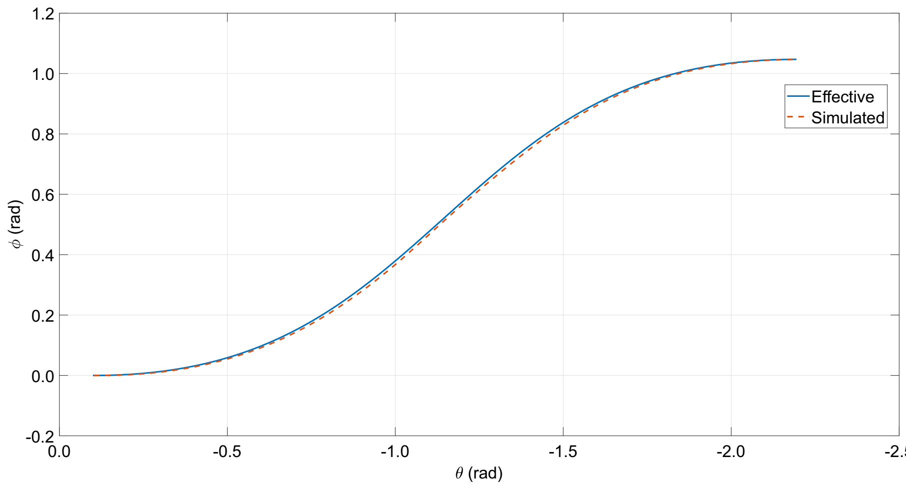

Fig. 16. Comparison between the nominal effective angular position of the driven wheel and the proposed method.

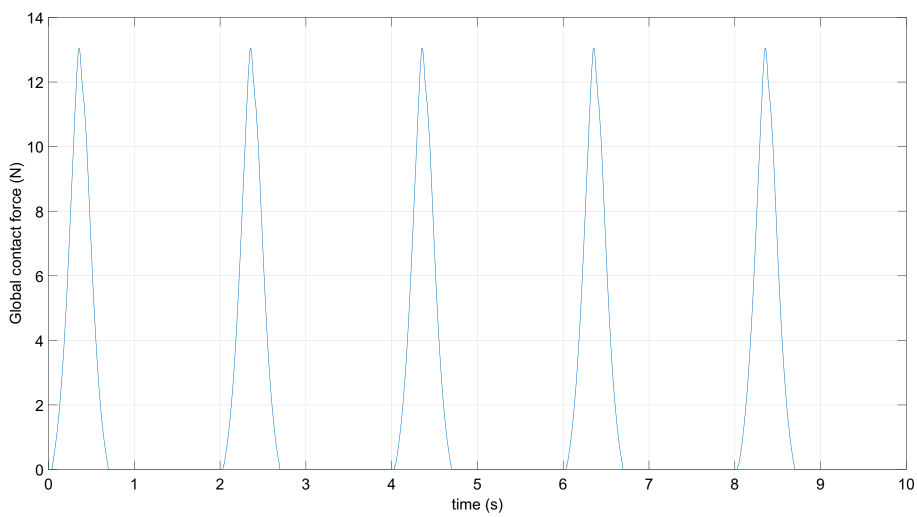

Fig. 17. Global contact force exchanged between the driving and driven wheels during the simulation.

where n represents the number of samples over the engagement cycle. The low RMS error of 1.13% confirms that, despite the time delay in contact initiation, the penalty-based contact formulation accurately captures the kinematic transmission characteristics of the mechanism throughout the engagement cycle.

Fig. 17 illustrates the time history of the contact force exchanged between the driving and driven bodies throughout the simulation interval. The plot highlights the intermittent nature of the interaction, with contact forces peaking during engagement and dropping to zero during disengagement phases.

Finally, Fig. 18 shows the distribution of the nodal contact forces on the driving and driven wheels at a specific time instant during the engagement phase, when the pin pushes against the slot and causes the driven wheel to rotate. It can be observed that the mesh discretization of the driven wheel is not uniform along the slot perimeter. This non-uniformity directly affects the magnitude of the nodal forces: higher values occur in regions of greater penetration and where the tributary area is larger, consistent with the formulation described in Section 2.

To assess the computational performance of the simulations, a parametric study was conducted by varying the time step size of the integrator over a simulation interval of 1 s, corresponding to the occurrence of the first contact event. The results are summarized in Fig. 19, where the total CPU time and the mean number of Newton-Raphson iterations per time step are reported. As the time step decreases, the mean number of iterations reduces. This behavior is expected: smaller time steps result in smaller incremental changes in the system state, providing a better initial guess for the Newton-Raphson solver and thus requiring fewer iterations to achieve convergence. However, reducing the time step also increases the total number of steps required to complete the simulation, which tends to increase the overall CPU time. Conversely, larger time steps reduce the number of integration steps but lead to greater incremental changes in the system configuration. This makes convergence more difficult, as reflected by the increasing number of iterations observed for $h > 4 \cdot 10^{-4}$ (s).

The interplay between these two effects produces a characteristic U-shaped curve for the CPU time: at small time steps, the computational cost is dominated by the large number of integration steps; at large time steps, it is dominated by the increased number of iterations required for convergence. An optimal time step of approximately $h = 4 \cdot 10^{-4}$ (s) is identified, where the total CPU time reaches its minimum value.

The time history of the number of iterations is further detailed in Fig. 20 for three representative cases: $h = 2 \cdot 10^{-4}$ (s), $h = 5 \cdot 10^{-4}$ (s), and $h = 8 \cdot 10^{-4}$ (s). The plot is limited to $t = 0.8$ (s), as the contact phase ends before this time. Smaller time steps require a significantly lower

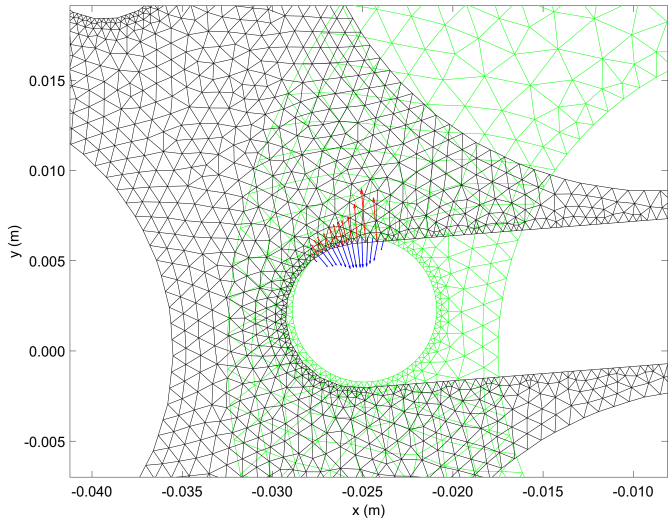

Fig. 18. Magnified view of the contact region between the pin and the slot of the driven wheel, showing the distribution of nodal contact forces along the perimeters of both bodies.

number of iterations throughout the simulation compared to larger time steps, confirming the trends observed in Fig. 19.

3.5. Ordinary gearbox

As a final example, we have simulated the contact between two cylindrical gears with an involute profile in an ordinary gearbox, as shown in Fig. 21. A pinion with radius $R_1 = 23$ (mm) and number of teeth $z_1 = 23$ is paired with a crown wheel with radius $R_2 = 57$ (mm) and number of teeth $z_2 = 57$. The pressure angle between the two gears is $\theta = 20°$, while the transmission ratio is $\tau = z_1/z_2 = 23/57 \approx 0.4035$. Structural and inertial parameters are reported in Table 5. This example has been selected to verify that the proposed model can simulate multiple contacts; in fact, during normal operation, the number of teeth in contact is approximately 1.9818, meaning that two pairs of teeth are in contact 98.18% of the time, while only one pair is in contact for the remaining 1.82% [45].

Both gear bodies are discretized using a uniform triangular mesh with an edge size of 0.6 (mm) along the perimeters. The pinion is driven by a prescribed angular motion consisting of a linear velocity ramp during the transient phase, from $t = 0$ to $t = 0.2$ (s), followed by a constant angular velocity of 600 (rpm) at steady state. The penalty coefficient $k_p = 6 \cdot 10^8$ was determined through a parametric study: higher values

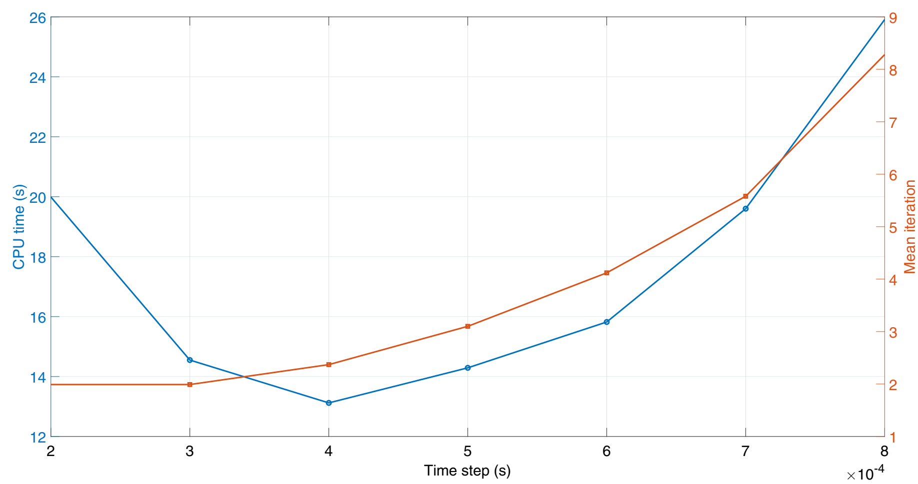

Fig. 19. Influence of the time step size on computational performance: total CPU time and mean number of iterations per time step.

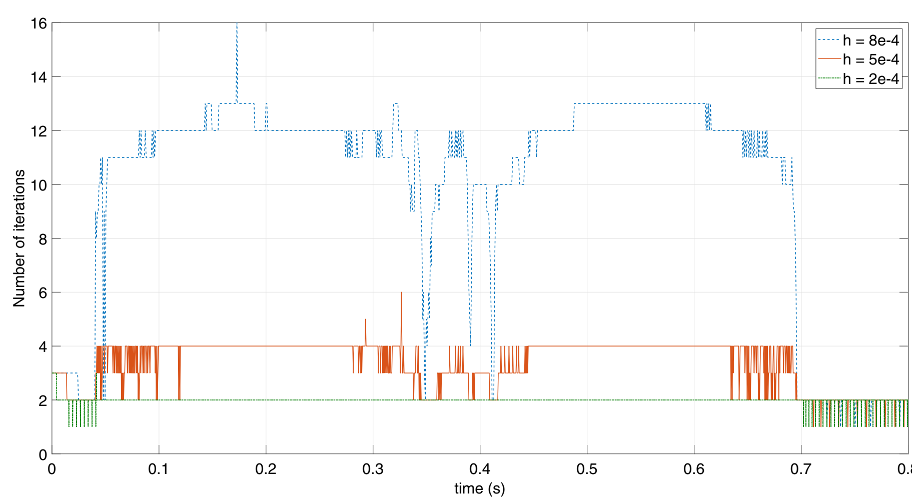

Fig. 20. Time history of the number of iterations for three different time step sizes: $h = 2 \cdot 10^{-4}$ (s), $h = 5 \cdot 10^{-4}$ (s), and $h = 8 \cdot 10^{-4}$ (s).

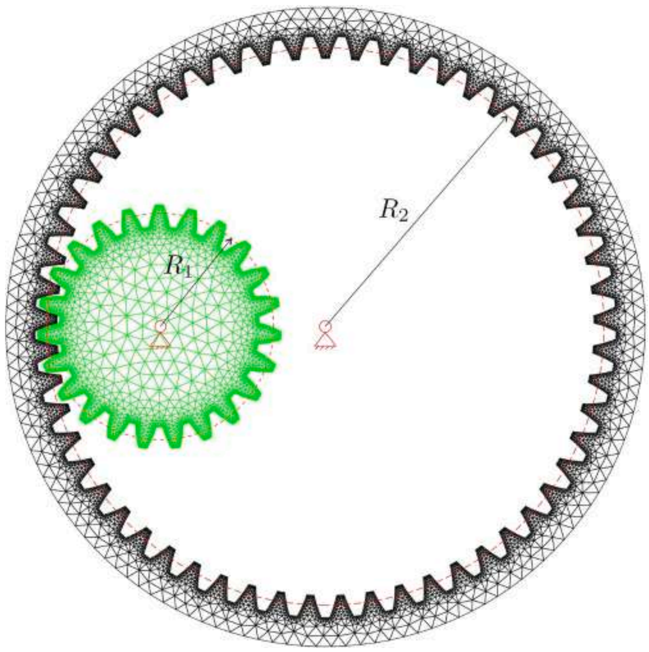

Fig. 21. Initial configuration of the ordinary gearbox. The pinion, shown in green, drives the crown wheel, shown in black.

Table 5
Gear structural parameters.

Young module E (Pa)	Poisson ratio ν	thickness t (mm)	mass density ρ (kg/m^3)	penalty coefficient k_p
207×10^9	0.29	50	7800	6×10^8

produced impulsive forces that led to unstable and erratic mechanism behavior, whereas lower values resulted in excessive penetration between the two bodies, yielding physically unrealistic configurations. Additionally, a damping coefficient of 0.4 (Nms/rad) was introduced in the crown wheel to ensure angular stability. This value was selected through a sensitivity analysis at fixed mesh resolution, by varying the damping coefficient from 0.15 to 2 (Nms/rad) and evaluating the resulting mean values of the pressure angle and transmission ratio. As shown in Fig. 22, the optimal damping value corresponds to the point closest to the intersection of the nominal values $\theta_{ideal} = 20°$ and $\tau_{ideal} = 0.4035$.

Based on these parameters, a series of simulations were performed to assess the precision and robustness of the proposed method. The global contact forces $\mathbf{F}_s$ and $\mathbf{F}_m$ exchanged between the teeth of the crown wheel and the pinion are shown in Fig. 23, depicted in green and red, respectively. The simulation corresponds to the case of flexible bodies, as evidenced by the mesh visualization with a color scale representing the nodal displacements at a specific time instant. In particular, the color scale for the pinion is displayed on the left side, while that for the crown wheel is shown on the right side.

A magnified view of the local contact interaction between two meshing teeth is provided in Fig. 24. The distribution of the nodal forces along the perimeters of both bodies, calculated according to the algorithm described in Section 2, can be clearly appreciated. Since the mesh is uniformly distributed, larger force magnitudes correspond to regions of greater penetration. An exception occurs for nodes adjacent to an intersection point, where the tributary area may be smaller than nominal, as can be observed in the figure.

The kinematic behavior of the mechanism was further investigated by analyzing the angular velocities of both bodies. The time histories of the pinion and the crown wheel angular velocities over the entire simulation interval, from $t = 0$ to $t = 0.5$ (s), are reported in Fig. 25. To evaluate the transmission ratio at steady state, the ratio $\tau = \omega_{out}/\omega_{in}$ was computed by averaging over the interval from $t = 0.2$ (s) to $t = 0.5$ (s), corresponding to the steady-state regime. The resulting mean value is $\bar{\tau} = 0.4035$, which matches the theoretical value reported above.

To quantify the instantaneous deviations from the ideal transmission ratio, the following relative root-mean-square error (RMSE) was employed:

$$\varepsilon_\tau = \frac{1}{\tau_{ideal}} \sqrt{\frac{1}{n} \sum_{i=1}^{n} \left(\tau_i - \tau_{ideal}\right)^2} \times 100 \tag{42}$$

where τ_i denotes the instantaneous transmission ratio at the i-th time step, $\tau_{ideal} = 23/57$ is the theoretical value, and n is the number of samples in the steady-state interval. The computed error for the selected mesh size of 0.6 (mm) is $\varepsilon_\tau = 0.3137\%$, confirming the accuracy of the

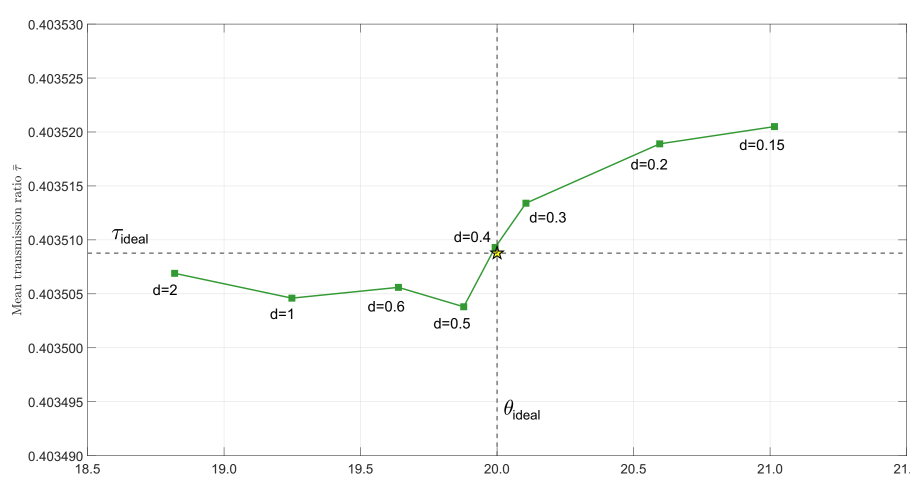

Fig. 22. Sensitivity analysis of the damping coefficient: mean transmission ratio $\bar{\tau}$ versus mean pressure angle $\bar{\theta}$ for different damping values. The dashed lines indicate the theoretical values, and the star marker denotes the optimal configuration at $d = 0.4$ Nms/rad.

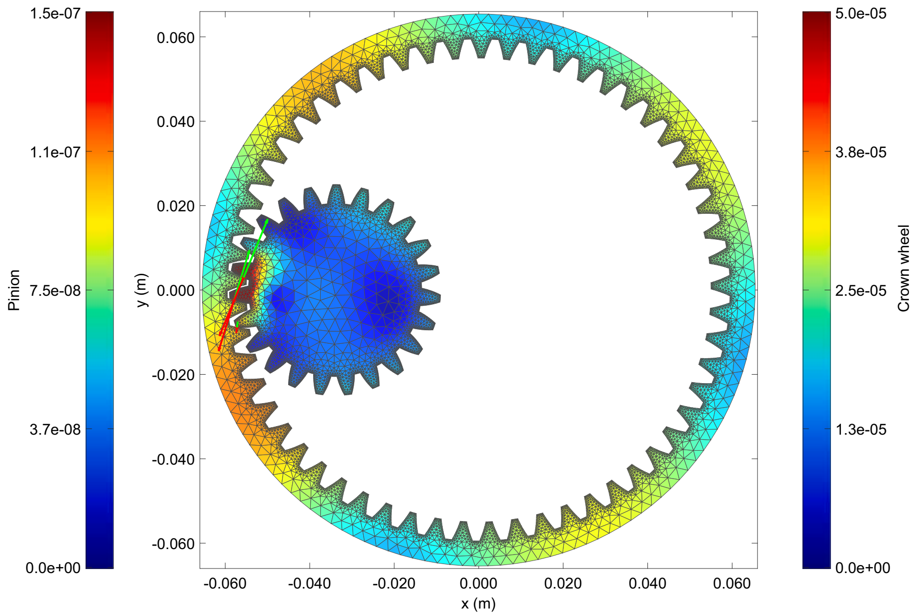

Fig. 23. Global contact forces between the pinion and crown wheel teeth. The forces acting on the pinion are shown in red, while those on the crown wheel are depicted in green. The color maps represent the nodal displacement magnitude for each gear.

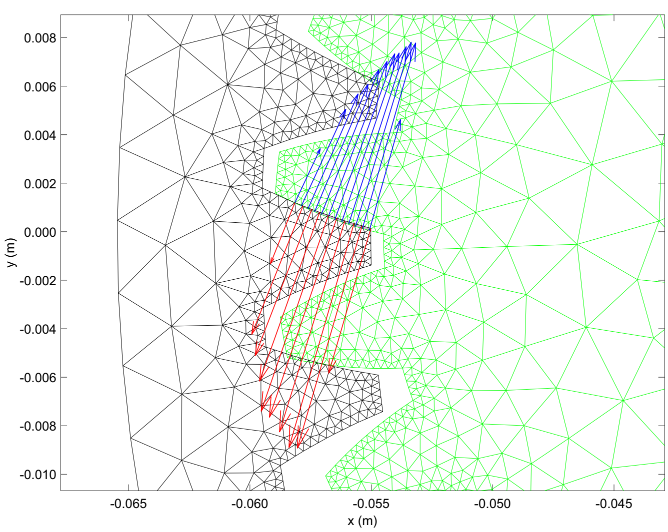

Fig. 24. Magnified view of the contact region between two meshing teeth, showing the distribution of nodal contact forces along the perimeters of both bodies.

proposed contact formulation in reproducing the expected kinematic behavior.

The precision of the contact formulation was further evaluated by examining the evolution of the pressure angle. Analytically, in a contact between two spur gears with involute profiles, the pressure angle θ should remain constant for each engaging tooth pair, with the resultant force aligned along the line of action. As shown in Fig. 23 for the three contact pairs, the most significant deviations from the nominal 20° value occur at the beginning and end of the contact path. These fluctuations correspond to the points where the tooth tip enters or exits the flank of the mating gear. Conversely, the angle remains stable and close to the nominal value throughout the central portion of the engagement, where the transmitted force reaches its maximum.

The time history of the simulated pressure angle, compared to the nominal value of 20°, is reported in Fig. 26. During the initial transient phase, the system exhibits significant oscillations. This behavior is attributed to the fact that, at the beginning of the simulation, the gear teeth are not yet in contact. When the velocity ramp is applied to the pinion, the two bodies suddenly engage, and the mechanism responds with a pronounced dynamic transient characterized by large amplitude fluctuations.

As the simulation progresses and the system reaches steady state, after $t = 0.2$ (s), the pressure angle oscillates around the nominal value with a considerably reduced amplitude. These residual oscillations are inherent to the penalty-based contact formulation, which allows penetration between the contacting bodies. This penetration introduces small deviations from the ideal kinematic behavior, causing the computed pressure angle to fluctuate about its theoretical value rather than remaining exactly constant.

Finally, a mesh sensitivity analysis was performed to evaluate how the mesh size affects the accuracy of the numerical results. As reported in Fig. 27 and Table 6, refining the mesh leads to a progressive reduction in the transmission ratio error. This trend confirms the expected convergence behavior as the number of mesh elements increases, with the numerical solution progressively approaching the analytical result, thus confirming the accuracy of the proposed method.

Following the same analysis performed for the Geneva mechanism, Fig. 28 reports the time history of the number of iterations required for convergence at each time step for two different time step sizes.

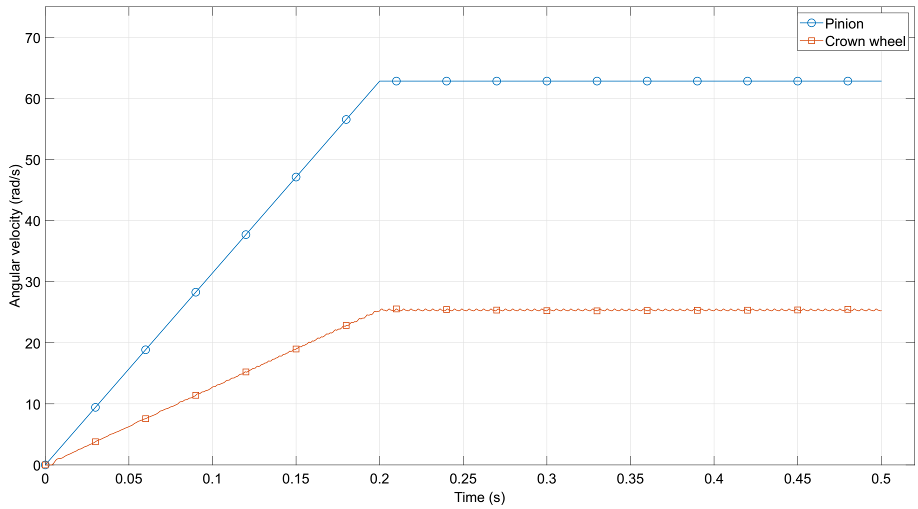

Fig. 25. Angular velocities of the pinion (blue) and crown wheel (red) throughout the simulation interval.

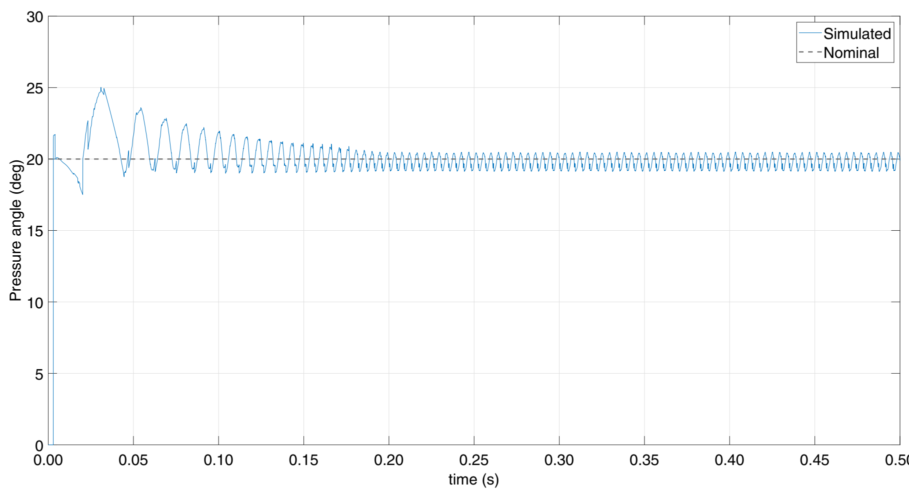

Fig. 26. Time evolution of the pressure angle. The simulated value, shown as the solid blue line, oscillates around the nominal value of 20°, represented by the dashed black line.

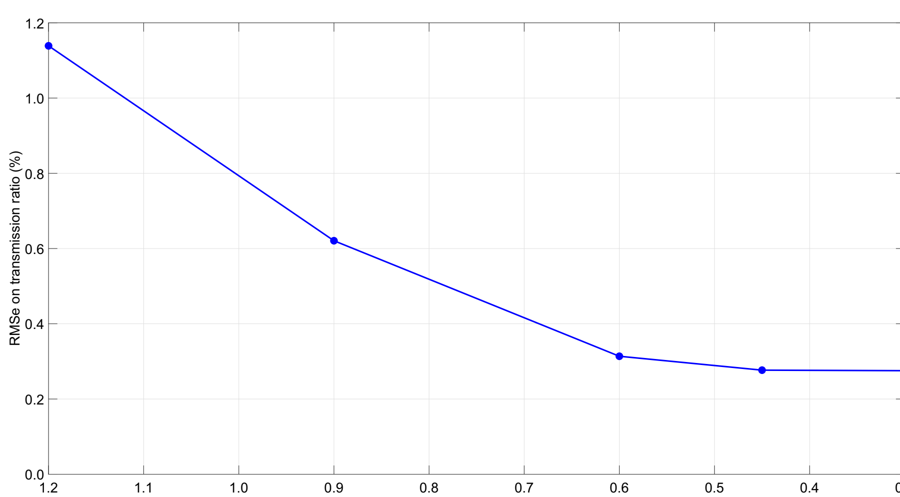

Fig. 27. Mesh sensitivity analysis: RMSE of the transmission ratio as a function of the mesh size.

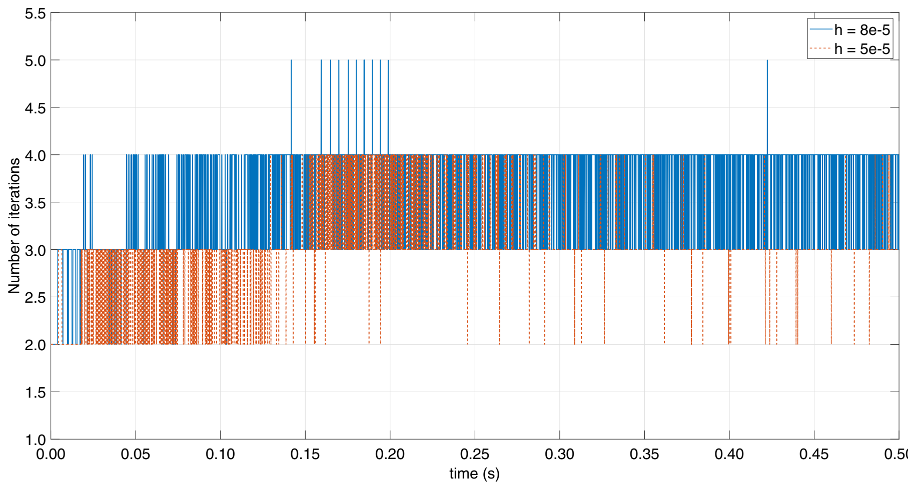

Fig. 28. Time history of the number of iterations for two different time step sizes: $h = 5 \cdot 10^{-5}$ (s) and $h = 8 \cdot 10^{-5}$ (s).

Table 6
Mesh sensitivity analysis: RMSE of the transmission ratio for different mesh sizes.

Mesh size (mm)	RMSe (%)	Simulation time (s)
1.20	1.1388	48.89
0.90	0.6208	62.32
0.60	0.3137	100.28
0.45	0.2767	146.67
0.30	0.2753	219.66

4. Discussion and conclusions

This work introduces a novel contact formulation for planar multibody systems, employing a penalty approach that leverages the intersection area between contacting bodies to determine the global contact force. The proposed methodology directly utilizes the geometric overlap to compute both the magnitude and direction of the contact interaction. The resultant force is applied at the centroid of the contact region, with its magnitude scaled proportionally to the intersection area. Its direction is established through a weighted average of the outward unit normal vectors at the boundary nodes; this weighting scheme consistently accounts for both tributary areas and local nodal indentation distances to ensure a physically grounded force distribution. This global contact force is then decomposed and distributed to the contact nodes, ensuring equilibrium and preserving its direction. A first relevant aspect is that the proposed method is symmetric with respect to the two bodies in contact, and therefore, the definition of master and slave can also be eliminated. Another significant advantage is that the proposed method inherently resolves the Closest Point Projection (CPP) problem without requiring specific treatments for singular or irregular cases. Conventionally, the CPP procedure relies on the differentiability of the surface parametrization; however, at the discrete level, the common issue of normal discontinuities at nodes is overcome. By ensuring a uniquely defined contact normal at every boundary point, the formulation maintains numerical robustness even in the presence of non-smooth geometries.

An initial comparison demonstrated the method's ability to faithfully reproduce the results of Hertzian theory. The formulation was then benchmarked against the STS method. The proposed method proved highly accurate, yielding results comparable to STS across various mesh densities. Furthermore, computational performance tests revealed that the contact algorithm consistently outperforms STS. This efficiency stems from its top-down architecture: all nodes within the intersection zone are identified in the initial phase and treated collectively as a single contact entity.

A classic patch test was subsequently employed to verify the uniformity of the normal contact pressure under varying nodal distributions and penetration depths. The results demonstrate that the nodal force distribution is directly governed by the tributary areas, accurately reflecting contact physics where higher nodal densities lead to lower individual forces. While the contact pressure remains uniform, a discrepancy persists between the master and slave bodies due to the asymmetrical positioning of their respective intersection nodes. Although this inherent penalty-method error cannot be eliminated, it can be mitigated by increasing the penalty stiffness. However, a trade-off is required: while high stiffness minimizes penetration, it must be balanced against the risk of numerical instabilities and overly impulsive responses during impacts.

The Geneva mechanism was then utilized to assess the influence of impacts and flexibility on the dynamics of a precision system. The findings were consistent with theoretical expectations. As anticipated, the interpenetration inherent in the penalty formulation introduces a minor delay in the driven response, which nevertheless remains within acceptable limits.

Finally, an ordinary gearbox was analyzed to evaluate the method's performance in scenarios involving multiple simultaneous contacts. The formulation proved reliable in replicating key features, such as the transmission ratio and the pressure angle. In the latter case, the penalty approach introduces small fluctuations around the nominal values due to the interpenetration between the tooth tip and flank. A sensitivity analysis across different mesh densities confirmed that the results remain robust and consistent with theoretical predictions, even when using coarser meshes.

Future developments will focus on incorporating friction forces into the proposed formulation. The integration of tangential contact forces will enable a more detailed representation of contact interactions, allowing the method to capture stick–slip phenomena and energy dissipation.

CRediT authorship contribution statement

Pietro Davide Maddio: Writing – review & editing, Writing – original draft, Software, Methodology, Data curation, Conceptualization. **Rosario Sinatra:** Validation, Supervision. **Alessandro Cammarata:** Writing – review & editing, Writing – original draft, Software, Methodology, Data curation, Conceptualization.

Declaration of competing interest

The authors declare that they have no known competing financial interests or personal relationships that could have appeared to influence the work reported in this paper.

Acknowledgements

This research was supported by the Pia.ce.ri. Starting Grant, Line of Intervention 2025, University of Catania, within the project CONTACT.

Data availability

No data was used for the research described in the article.

References

[1] Wriggers P, Laursen TA. Computational contact mechanics, vol. 2. Springer; 2006.
[2] Popp A, Wriggers P. Contact modeling for solids and particles, vol. 585. Springer; 2018.
[3] Francavilla A, Zienkiewicz OC. A note on numerical computation of elastic contact problems. Int J Numer Methods Eng 1975;9(4):913–24.
[4] Taylor RL, Papadopoulos P. On a patch test for contact problems in two dimensions. Computational methods in nonlinear mechanics 1991;690:702.
[5] Hughes TJR, Taylor RL, Sackman JL, Curnier A, Kanoknukulchai W. A finite element method for a class of contact-impact problems. Comput Methods Appl Mech Eng 1976;8(3):249–76.
[6] Bathe K-J, Chaudhary A. A solution method for planar and axisymmetric contact problems. Int J Numer Methods Eng 1985;21(1):65–88.
[7] Wriggers P, Simo J. A note on tangent stiffness for fully nonlinear contact problems. Commun Appl Numer Methods 1985;1(5):199–203.
[8] Hallquist JO, Goudreau GL, Benson D. Sliding interfaces with contact-impact in large-scale lagrangian computations. Comput Methods Appl Mech Eng 1985;51(1–3):107–37.
[9] Wriggers P, Van TV, Stein E. Finite element formulation of large deformation impact-contact problems with friction. Comput Struct 1990;37(3):319–31.
[10] Papadopoulos P, Jones RE, Solberg JM. A novel finite element formulation for frictionless contact problems. Int J Numer Methods Eng 1995;38(15):2603–17.
[11] Stupkiewicz S. Extension of the node-to-segment contact element for surface-expansion-dependent contact laws. Int J Numer Methods Eng 2001;50(3):739–59.
[12] El-Abbasi N, Bathe K-J. Stability and patch test performance of contact discretizations and a new solution algorithm. Comput Struct 2001;79(16):1473–86.
[13] Kim JH, Lim JH, Lee JH, Im S. A new computational approach to contact mechanics using variable-node finite elements. Int J Numer Methods Eng 2008;73(13):1966–88.
[14] Kang S-H, Lee S-M, Shin S. Improved area regularization technique for penalty-method-based node-to-segment contact analysis. Comput Mech 2023;71(4):801–25.
[15] Zavarise G, De Lorenzis L. The node-to-segment algorithm for 2d frictionless contact: classical formulation and special cases. Comput Methods Appl Mech Eng 2009;198(41–44):3428–51.
[16] Sun C, Liu GR, Huo SH, Wang G, Yu C, Li Z. A novel node-to-segment algorithm in smoothed finite element method for contact problems. Comput Mech 2023;72(5):1029–57.
[17] Simo JC, Wriggers P, Taylor RL. A perturbed lagrangian formulation for the finite element solution of contact problems. Comput Methods Appl Mech Eng 1985;50(2):163–80.
[18] Papadopoulos P, Taylor RL. A mixed formulation for the finite element solution of contact problems. Comput Methods Appl Mech Eng 1992;94(3):373–89.
[19] Batistić I, Cardiff P, Tuković Ž. A finite volume penalty based segment-to-segment method for frictional contact problems. Appl Math Model 2022;101:673–93.
[20] Belgacem FB. The mortar finite element method with Lagrange multipliers. Numer Math 1999;84:173–97.
[21] McDevitt T, Laursen T. A mortar-finite element formulation for frictional contact problems. Int J Numer Methods Eng 2000;48(10):1525–47.
[22] Wohlmuth BI. A mortar finite element method using dual spaces for the Lagrange multiplier. SIAM J Numer Anal 2000;38(3):989–1012.
[23] Puso MA. A 3d mortar method for solid mechanics. Int J Numer Methods Eng 2004;59(3):315–36.
[24] Fischer KA, Wriggers P. Frictionless 2d contact formulations for finite deformations based on the mortar method. Comput Mech 2005;36:226–44.
[25] Farah P, Popp A, Wall WA. Segment-based VS. Element-based integration for mortar methods in computational contact mechanics. Comput Mech 2015;55:209–28.
[26] Liu WN, Huemer T, Eberhardsteiner J, Mang HA. Modified node-smoothing method of non-smooth surfaces in FE analyses of 2d contact. Comput Struct 2002;80(27–30):2185–93.
[27] Alart P, Curnier A. A mixed formulation for frictional contact problems prone to newton like solution methods. Comput Methods Appl Mech Eng 1991;92(3):353–75.
[28] Cavalieri FJ, Cardona A. An augmented lagrangian technique combined with a mortar algorithm for modelling mechanical contact problems. Int J Numer Methods Eng 2013;93(4):420–42.
[29] Khulief YA. Modeling of impact in multibody systems: an overview. J Comput Nonlinear Dyn 2013;8(2):021012.
[30] Flores P, Lankarani HM. Contact force models for multibody dynamics, vol. 226. Springer; 2016.
[31] Nikravesh P. Planar multibody dynamics: formulation, programming with MATLAB®, and applications. CRC Press; 2018.
[32] Acary V, Brogliato B. Numerical methods for nonsmooth dynamical systems: applications in mechanics and electronics. Springer Science & Business Media; 2008.
[33] Studer C. Numerics of unilateral contacts and friction: modeling and numerical time integration in non-smooth dynamics, vol. 47. Springer Science & Business Media; 2009.
[34] Kazaz L, Pfister C, Ziegler P, Eberhard P. Transient gear contact simulations using a floating frame of reference approach and higher-order ansatz functions. Acta Mech 2020;231(4):1337–50.
[35] Rückwald T, Held A, Seifried R. Hierarchical refinement in isogeometric analysis for flexible multibody impact simulations. Multibody Syst Dyn 2023;57(3):343–63.
[36] Wang Q, Tian Q, Hu H. Dynamic simulation of frictional contacts of thin beams during large overall motions via absolute nodal coordinate formulation. Nonlinear Dyn 2014;77:1411–25.
[37] Wang Q, Tian Q, Hu H. Dynamic simulation of frictional multi-zone contacts of thin beams. Nonlinear Dyn 2016;83:1919–37.
[38] Sun D, Liu C, Hu H. Dynamic computation of 2d segment-to-segment frictionless contact for a flexible multibody system subject to large deformation. Mech Mach Theory 2019;140:350–76.
[39] Konyukhov A, Izi R. Introduction to computational contact mechanics: a geometrical approach. John Wiley & Sons; 2015.
[40] Konyukhov A, Schweizerhof K. Computational contact mechanics: geometrically exact theory for arbitrary shaped bodies, vol. 67. Springer Science & Business Media; 2012.
[41] Benson DJ, Hallquist JO. A single surface contact algorithm for the post-buckling analysis of shell structures. Comput Methods Appl Mech Eng 1990;78(2):141–63.
[42] Arnold M, Brüls O. Convergence of the generalized-α scheme for constrained mechanical systems. Multibody Syst Dyn 2007;18(2):185–202.
[43] Cammarata A, Pappalardo CM. On the use of component mode synthesis methods for the model reduction of flexible multibody systems within the floating frame of reference formulation. Mech Syst Signal Process 2020;142:106745.
[44] Johnson KL. Contact mechanics. Cambridge University Press; 1987.
[45] Budynas RG, Nisbett JK, et al. Shigley's mechanical engineering design, vol. 9. McGraw-Hill New York; 2011.